UNIVERSITÀ DEGLI STUDI DI PADOVA

Dipartimento di Fisica e Astronomia "Galileo Galilei"

Master Degree in Physics

Final Dissertation

A NOVEL NEUTRON DETECTOR FOR SOIL MOISTURE ESTIMATION OVER LARGE AREA

Thesis supervisor	Candidate
Prof. Luca Stevanato	Matteo Polo
Thesis co-supervisor	
Prof. Marcello Lunardon	

Academic Year 2019/2020

Abstract

The main goal of my thesis work is to characterize a novel neutron detector for soil moisture estimation. Nowadays due to climate change and population increasing, the correct management of the water resources is extremely important. For this reason in agriculture is necessary to develop an instrument that are able to determine soil moisture over large area in order to optimize water consumption. Several techniques are proposed in the past from point-scale to remote sensing.

In the last decade, a proximal geophysical method has been developed in order to fill the gap between point-scale and remote sensing approaches. The technique is called cosmic ray neutron sensing (CRNS) and it is based on the natural neutrons detected on the earth's surface that are mostly generated by cosmic rays, according to various processes. The fast neutron rate is anti correlated with the soil moisture content due to the great capacity of hydrogen present in water to thermalize fast neutrons. State-of-the-art probes used in CRNS are based on ^{3}He proportional counter tubes. ^{3}He is a nuclide produced almost entirely in artificial contexts as sub-product of the tritium decay, the current storage is depleting and the price is high and rising.

In my thesis, a new solution is studied. I use a novel detector based on zinc-sulfide inorganic scintillator doped with lithium (Ej-426). The light generated by the scintillator is collected and send to the photo-multiplier tube (PMT) by a wavelength shifter (Ej-280). The readout is made of a 1 inch photo-multiplier from Hamamatsu, a fast digitizer DT5725 from CAEN, and low-cost, low-power, embedded computer BeagleBone black.

In the first part of the work I focused my attention on discrimination algorithm in order to find the optimal filter that I can use to select correctly the event generated by neutrons and discard noise events. Then, I use this filter in a data acquisition, made in Casalserugo (-PD-) from August 2019 to December 2019. The results of this analysis show how the neutron counts is correlated with soil moisture content. After that, I study the response of the detector in function of the temperature by putting the scintillator and the photo-multiplier in a climate chamber. As I expect the neutron rate decrease when the temperature increase, this effects is due to the gain change of the PMT. The data acquired in the climate chamber are useful to correct the neutron rate in the field.

Another important aspect of the CRNS is that the neutron rate must be correct by the incoming flux of cosmic ray, for this reason, near the neutron detector we put a plastic scintillator in order to detect cosmic muons and try to use the muon rate to correct the neutrons counts. In the future the system will be improved in order to determine also the biomass. The farmers can to carry out the appropriate treatments fertilization works and phytosanitary treatments if they have detailed information about crop growth.

Contents

Chapter 1

Introduction

1.1   The importance of soil moisture estimation

Water is at the core of sustainable development and is critical for socio-economic development, energy and food production, healthy ecosystems and for human survival itself. As we can see in figure 1.1, only a small amount of all the water resource are "fresh water resources" that could be used for drinking, hygiene, agriculture and industry.
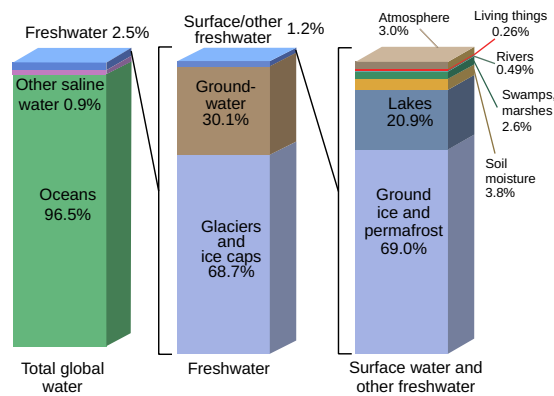
Figure 1.1: A graphical distribution of the locations of water on Earth [Shiklomanov, 1998]

For this reason, nowadays water sensing is very important in order to be able to manage correctly water resources. The precise knowledge of soil moisture can be useful in a lot of applications, for example in monitor drought, assist crop productivity, weather forecasting, floods prediction and in general water management [Entekhabi et al., 2014].

1.1.1 Soil moisture in agriculture

Nowadays, on average, agriculture accounts for 70% of global freshwater withdrawals. FAO (Food and Agriculture Organization) estimate that food production will increase by more than 50 percent by 2050, but the amount of water withdrawn by agriculture can increase by only 10 percent [Nations, 2018].It will be necessary to introduce a whole-farm management approach using information technology, satellite positioning data, remote sensing and proximal data gathering. The sector that uses this data for the optimization of agricultural production is called Precision Agriculture (PA) [Zarco-Tejada et al., 2014]. In PA one information that can be useful in resource management is the precise knowledge of the soil moisture content and the knowledge of water storage in crops biomass.

The soil moisture controls the rates of rainfall infiltration, deep percolation and run-off generation. Soil moisture controls also the dynamics of terrestrial ecosystems, especially in conditions of scarce water availability. In such environments, the rates of transpiration, carbon assimilation, and biomass production are often limited by the soil water content during the growing season. In these conditions of water-limited transpiration, vegetation undergoes a state of water stress, which depends (in terms of duration and frequency) on the plant physiology and the local pedological and climatic characteristics. The nutrient cycle and the budget of organic matter in the soil are also strongly affected by the dynamics of soil moisture. [Porporato et al., 2002].

The estimation of biomass production has a prominent role in the strategies to increase crop productivity and improve management efficiency. Monitoring biomass production is a diagnostic tool for the evaluation of crop management because the accumulation of biomass responds to the coupled effects of climate crop genomics, and nutrient/water management. The evaluation of biomass production during the growing cycle has interesting application for the assessment of the fertilization necessities, essential in the strategies of nitrogen variable doses in coordination with the diagnosis tools for remote estimation of nitrogen concentration. In addition, biomass accumulation is strongly related to yield production in grain crops although not in an unequivocal way [Campos et al., 2018].

For this reason a continuous evaluation of soil moisture content and biomass determination can be useful for a precise programming of irrigation and fertilizing interventions in order to reducing environmental impacts.

1.1.2 Soil moisture in hydrology

Soil moisture is a key variable for the partitioning of rainfall into infiltration and outflow thus playing a fundamental role in run-off modelling and flood forecasting [Brocca et al., 2017]. Several studies employed in situ soil moisture observations for enhancing:

- the estimation of initial conditions in flood modelling [Massari et al., 2014, Tramblay et al., 2010]

- the calibration of hydrological models [Wooldridge et al., 2003]

- flood simulation through data assimilation approaches [Aubert et al., 2003]

Moreover in literature is reported that soil moisture observations play an important role for the mitigation of many natural hazards [Brocca et al., 2017]. For example [Brocca et al., 2012] demonstrated that the soil moisture detection is able to improve the performances of a statistical regression model aimed at predicting the temporal evolution of landslide movement for a small landslide in central Italy.

1.1.3 Soil moisture in climate science

Soil moisture plays an important role of land energy and and water balance through its impact of evapotranspiration (E). Evapotranspiration is a major component of the continental water cycle, since it returns as much as 60% of the whole land precipitation back to the atmosphere. In addition, evapotranspiration is also an important energy flux: the energy required for evaporating a given mass of liquid water corresponds to approximately 600 times the energy required to increase its temperature by 1K, and to 2400 times the energy required to increase the temperature of a corresponding mass of air by 1K. Consequently, land evapotranspiration also uses up more than half of the total solar energy absorbed by land surfaces. Through its impact on the partitioning of the incoming energy in the latent and sensible heat fluxes, soil moisture has several additional impacts on climate processes, in particular on air temperature, boundary-layer stability and in some instances on precipitation [Seneviratne et al., 2010b]. In figure 1.2 is show how the soil moisture variation can affected the environmental temperature variation.
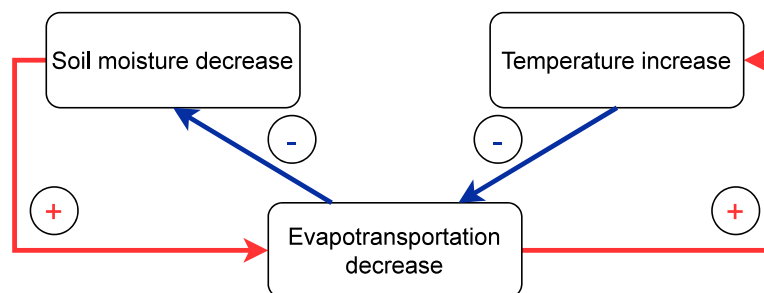
Figure 1.2: Processes contributing to soil moisture–temperature coupling and feedback loop. Positive arrows (red) indicate processes that lead to a drying/warming in response to a negative soil moisture anomaly and blue arrows denote potential negative feedbacks

1.2 Definition of water content

A definition of soil can be found in [Hillel, 1998], where it is define as the weathered and fragmented outer layer of the earth's terrestrial surface. The soil is composed by water, air, mineral and organic matter. We focus our attention on the water content. It is possible to define the water content of a soil in different way. The first is the gravimetric water content, define as

$$\theta_g = \frac{M_{water}}{M_{soil}} \tag{1.1}$$

where M_w is the mass of water and M_s the mass of soil. Another definition is given by the ratio of water volume and the total soil volume, called volumetric water content, equation 1.2.

$$\theta_v = \frac{V_{water}}{V_{soil}} \tag{1.2}$$

The two definitions are linked by the following relationship:

$$\theta_v = \theta_g \frac{\rho_{soil}}{\rho_{water}} \tag{1.3}$$

Where ρ_{soil} and ρ_{water} are respectively the soil bulk density and water density. Another important quantity is the actual maximum soil moisture content of a given soil volume. This maximum soil moisture content is defined as the saturation soil moisture content θ_{SAT}. Using θ_{SAT}, a further common definition of soil moisture is the saturation ratio:

$$\theta_S = \frac{\theta}{\theta_{SAT}} \tag{1.4}$$

with θ_S varying between 0 (no soil moisture) and 1 (full saturation), while θ varies between 0 and θ_{SAT} [Brocca et al., 2017]. As we can deduce θ express soil moisture in relative terms, i.e. as ratio of a given soil volume or water storage [m^3/m^3]. In some case is useful to define soil moisture in absolute terms (water depth [mm]). For this reason moisture content is often expressed as reported in the relation 1.5, where d is the soil depth.

$$S = d \cdot \theta \tag{1.5}$$

1.3   Soil moisture estimation

Due to the importance of soil moisture estimation, several method are developed in the last years. These techniques can be divide in two main category: in situ and remote sensing [Hillel, 1998]. In the first category it is necessary a direct contact with the soil, in this category we found gravimetric measurement [Robock, 2015] and the time domain reflectometry (TDR) technique [Robinson et al., 2003]. On the other hands we found the remote sensing estimation, that is the collection of information regarding an object of inter est, conducted from some distance without actual contact with that object. Remote sensing is a promising technique in environmental soil physics and hydrology. It permits measurements that are not generally possible with traditional techniques, especially in areas where on-site stations are sparse and where data are difficult to obtain otherwise [Hillel, 1998]. In this group we can found microwave remote sensing [Entekhabi et al., 2014, Schmugge et al., 2002], the Gravity Recovery and Climate Experiment (GRACE) [Tapley et al., 2004].

1.3.1   Gravimetric

The gravimetric method, also called the thermostat-weight technique, has been in use for a long time because is low-tech and simple [Robock, 2015]. Soil samples are taken using coring devices or augers at required depths and locations. The sample is weighed, oven-dried (usually at 105 °C) [Seneviratne et al., 2010a], and weighed again. The difference in mass gives the total soil moisture in the sample, which is converted to volumetric units using the density of the soil. While this method represents the actual "ground truth", there are several issues with this approach. The most important is that the measurement method is destructive, and can thus not be reproduced. Moreover, significant manpower is required for the retrieval of the samples and the laboratory measurements. For these reasons, the temporal resolution of long-term measurement networks using this technique is usually coarse, typically of the order of 1-2 weeks at best. Nonetheless, gravimetric measurements still represent the reference measurements for calibrating other soil moisture measurement methods, since all other approaches are indirect [Robock, 2015].

1.3.2   Time domain reflectometry

The time domain reflectometry (TDR) can be used for soil moisture estimation thanks to its ability to accurately measure the permittivity of a material and the fact that there is a good relationship between the dielectric permittivity (dielectric constant) of a material and its water content [Robinson et al., 2003]. One of the strengths of the TDR measurement method is that many probes can be monitored almost simultaneously using a multiplexer, so it is possible to monitoring large area. Time domain reflectometry

measures the propagation velocity of a step voltage pulse with a bandwidth of around 20 kHz to 1.5 GHz [Heimovaara, 1994]. The velocity of this signal is primarily a function of the permittivity of the material through which it travels with potential modification by conductive losses. Hence it follows that the permittivity can be determined by measuring the time that the wave takes to traverse the probe. In fact from the time of signal propagation (t) and length of transmission line (l) it is possible to derive the permittivity of the material using the equation 1.6, where c is the speed of light.

$$t = \frac{2l\sqrt{\epsilon_r}}{c} \tag{1.6}$$

An example of the TDR apparatus is show in figure 1.3. In the right panel of 1.3 are illustrates two waveforms, one in air and one in water due to the different permittivity of a material.
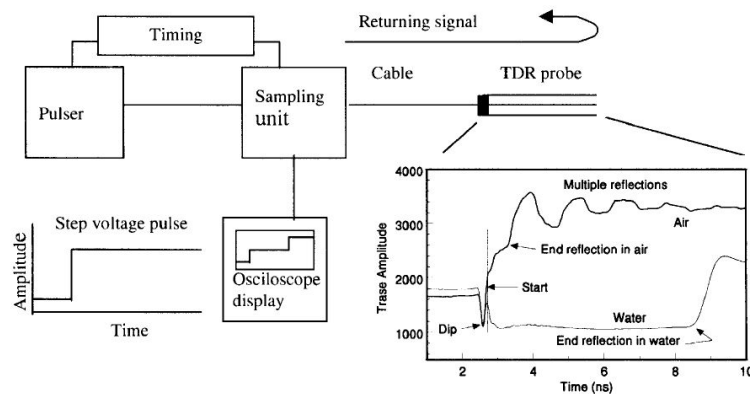
Figure 1.3: A schematic diagram of the TDR main components. [Robinson et al., 2003].

1.3.3 Microwave remote sensing

From solar radiation that is reflected and emitted by the land it is possible to extrapolate a lot of information. The reflected solar is used in hydrology for snow mapping vegetation/land cover and water quality studies. The thermal emission in the infrared is used for surface temperature and in the microwave for soil moisture and snow studies. At microwave frequencies the most striking feature of the emission from the earth's surface is large contrast between water and land. This emissivity contrast is due to the large dielectric constant of water (80) while that of most dry minerals or soils is less than 5, which causes an emissivity contrast of 0.4 for water to about 0.95 for dry land. When you have a mixture of water and dry soil the resulting dielectric constant is between these two extremes thus affording a mechanism for the remote sensing of the moisture content of soils by observing its emissivity at microwave frequencies [Schmugge et al., 2002].

One of the most important experiment that try to develop this technique is Soil Moisture

Active Passive (SMAP), run by NASA. The baseline science requirement for SMAP is to provide estimates of soil moisture in the top 5 cm of soil at 10 km spatial resolution and 3-day average intervals over the global land area, excluding regions of snow and ice, frozen ground, mountainous topography, open water, urban areas, and vegetation with water content greater than 5 kg m^{-2} [Entekhabi et al., 2014]. The main disadvantage of this technique is that it is limited at the first 5 cm of soil, while it is root-zone, i.e. 50-80cm, that soil moisture is relevant for most climate applications and agriculture [Seneviratne et al., 2010a].

1.3.4 Gravity Recovery and Climate Experiment (GRACE)

Gravity measurements can be used to determine temporal changes in the mass of a conceptual column of water in the near surface. Monthly gravity field estimates made by the twin Gravity Recovery and Climate Experiment (GRACE) satellites have a geoid height accuracy of 2 to 3 millimetres at a spatial resolution as small as 400 kilometres. Earth's gravity field reflects the composition and structure of the planet, including the distribution of the atmosphere and water mass on and below its surface. Observations of seasonal variations in Earth's gravity field place important constraints on models of global mass variability and temporal exchange among the land, ocean, and atmosphere. This is particularly important for subsystems that might otherwise be extremely difficult to detect and monitor (e.g., deep ocean currents and deep aquifers). Temporal variations of Earth's gravity field range in size from 10 to 100 parts per million (variation from the mean) and occur on a variety of time scales. [Tapley et al., 2004]. The main limitation is due to the low spatial resolution that is 400–500 km at best [Seneviratne et al., 2010a].

1.3.5 Proximal geophysical methods

The techniques that we describe in previous section have a different time and space resolution, as show in figure 1.4. In [Mahmood et al., 2013] is reported that for precision agriculture fine-scale spatial and time information on soil is needed.

Proximal gamma-ray spectroscopy has recently emerged as a promising tool to collect fine-scale soil information. In fact soil water content can be estimated in real time on the basis of temporal changes in gamma ray intensity to which soil moisture is negatively correlated [Strati et al., 2018]. A second method is based on the intensity of low-energy cosmic-ray neutrons above the ground, that is inversely correlated with soil water content. This approach is called Cosmic Ray Neutron Sensing (CRNS), and it is describe in detail in chapter 2.
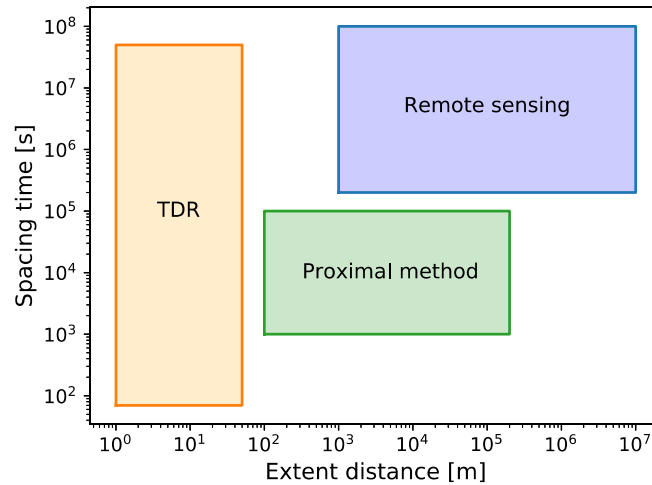
Figure 1.4: Time and space resolution of the different soil moisture estimation approach

1.4 Bio-mass estimation

In agricultural production, crop height, degree of coverage, and biomass density are important parameters for the assessment of crop stands. Based on these parameters, expected crop yields can be forecasted and the amount of fertilisers and pesticides for the site-specific crop management can be optimised [Ehlert et al., 2008].

Several methods for measuring crop height, degree of coverage, and biomass are reported in the literature. Sensors for measuring crop parameters with an acceptable accuracy and high reliability at a reasonable price are essential prerequisite to obtain this information. In [Ehlert et al., 2008] is described the possibility to estimate the crop biomass density by laser triangulation. Effective measuring range should span a minimum of 1.5 m to sense crops in all relevant growth stages. Furthermore, the sensors should be working in darkness as well as in bright sun light to provide 24 h accessibility. Another technique is proposed in [Ehlert et al., 2008], in witch a unmanned aerial vehicle (UAV) is used to determine plant height (PH). PH is positively correlated with crop biomass. In combination with a non-vegetation ground model, PH can be obtained by quantifying the height of a canopy using crop surface models.The main limitation was the influence of lodging cultivars in the later growth stages, producing irregular plant heights. Recently, [Tian et al., 2016a] proposed to use the ratio of thermal to fast neutron intensity measured with the CRNS probe to estimate aboveground biomass for maize and soybean crops. This technique is describe in the following chapter.

Chapter 2

Neutron detection for soil moisture estimation

The use of neutrons as a probe for soil moisture estimation was proposed by Zreda for the first time in 2008 [Zreda et al., 2008]. In the article is shown how soil moisture can be measured, over large area, from cosmic fast neutrons that are moderated mainly by hydrogen atoms, as show in figure 2.1. These neutrons are sensitive to water content changes, but largely insensitive to variations in soil chemistry. Their intensity above the surface is inversely correlated with hydrogen content of the soil.
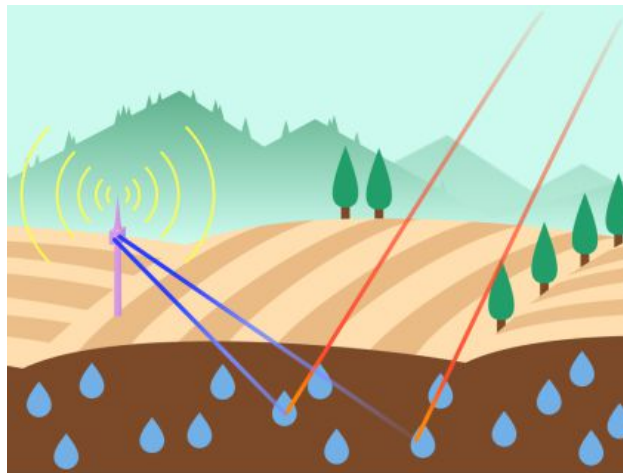
Figure 2.1: Fast neutrons from cosmic rays (red lines) are thermalized by the water stored in the soil. After the thermalization that neutron (blue lines) are detected by a neutron probe

2.1 Cosmic ray discovery

Since the 19th century has been know that radioactivity produces ionisation in the atmosphere. The ionisation rate was measured by charging a well-isolated electroscope and measuring its discharge time. In 1910–11, D. Pacini [Pacini, 1912], when measuring the discharge rate of an isolated electrometer at difference altitude discovered the existence of an ionisation source different from the radioactivity of the ground. He could not establish, however, whether this source was in the atmosphere or above it [Bettini, 2014]. In 1911 Victor Hess, using a hot balloon, see figure 2.2, took such measurements further.

In that years balloon reached an altitude of around 1100 metres, but Hess found "no essential change" in the amount of radiation compared with ground level. Then, on 7 April 1912, Hess made an ascent to 5300 metres during a near-total eclipse of the Sun. Hess still measured rising radiation at rising altitudes and he concluded that "The results of the observations seem most likely to be explained by the assumption that radiation of very high penetrating power enters from above into our atmosphere." [Hess, 1912]. In the 1920s, the term cosmic rays was coined by Robert Millikan who made measurements of ionization due to cosmic rays from deep under water to high altitudes and around the globe. In 1930, Bruno Rossi

Figure 2.2: Hess lands after his balloon flight in 1912 [Source:`www.cern.ch`]

predicted a difference between the intensities of cosmic rays arriving from the east and the west that depends upon the charge of the primary particles—the so-called "east-west effect". In fact different experiment found that the intensity is greater from the west, proving that most primaries are positive.

2.2 Cosmic ray composition

Cosmic ray can be divide in primary, that originate in various astrophysical processes, and the secondary that are created by the interaction of the primary cosmic ray with the atmosphere.

The primary composition, namely at the top of the atmosphere, consists of 85% protons, 12% α particles, 1% heavier nuclei and 2% electrons [Bettini, 2014], while the secondary are mainly composed by neutrons, gamma rays, muons and several short-lived subatomic particles have since been identified in the secondary cosmic-ray flux. Another way to

divide cosmic ray is based on energy. In fact cosmic flux cover a a very wide range, as show in figure 2.3. The origin of these changes in the steepness of the spectrum is still the
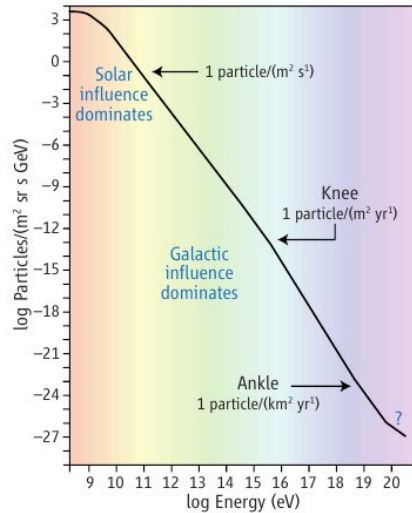
Figure 2.3: Cosmic ray flux in function of energy [Duldig, 2006]

subject of intense study, but it is assumed that they distinguish between populations of cosmic rays originating via different mechanisms. Current suggestions are that the cosmic rays with energies less than 10^{10} eV are primarily solar cosmic rays produced in solar flares and coronal mass ejections, while those with energies between 10^{10} eV and the knee at 10^{15} eV are galactic cosmic rays produced in the shocks of supernova remnants. The origin of the cosmic rays with energies between the knee and ankle is unclear. They are again thought to be produced within the Galaxy, but the energies are too high for them to be accelerated by the shocks of supernova remnants. The origin for the ultra-high energy cosmic rays below the ankle is also a mystery, but many have suggested that these may be created outside of our Galaxy.

2.3   Cosmic ray fast neutrons on Earth

The cosmic-ray neutrons found in the earth's atmosphere are essentially all generated by nuclear interactions of the primary and secondary cosmic rays in the outer part of the Earth's atmosphere, as show in figure 2.4. There is no evidence indicating any appreciable flux of neutrons in the primary radiation due to the short neutron half-life (881 s), so it is unlikely that a significant number of neutrons could reach the earth from regions more distant than the sun [Hess et al., 1959].

The intensity of high-energy neutrons varies in space and time. Spatial variations are due to the variable strength of the geomagnetic field. Temporal variations in cosmic-ray intensity are due to solar activity. Another variable that can change the intensity of high-
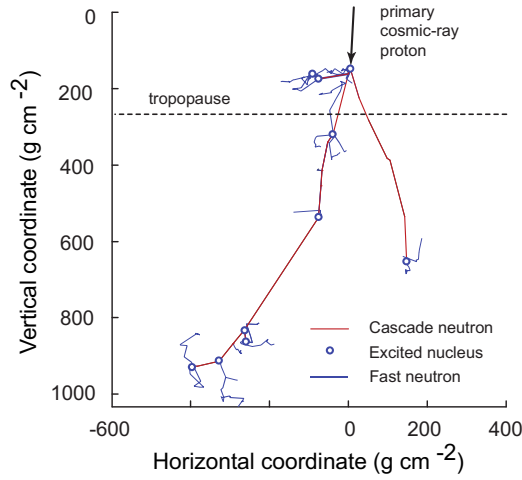
**Figure 2.4:** Cascade of high-energy secondary neutrons, and production and scattering of fast neutrons [Zreda et al., 2012]

energy neutrons is the barometric pressure, this dependence is describe in detail in section 2.5.

The earth's magnetic field forms a shield against charged particles everywhere except for particles entering vertically into a pole. As primary cosmic ray particles near earth, the magnetic field interacts with the particle's charge and bends the particle's trajectory. If the particle hits an atmospheric atom and starts a cascade, each of the cascade charged particles will also have its path bent. This bending both increases the possibility that the particles will end up going back out into space, and lengthens the cascade path, reducing the probability that particles will reach sea level. The effectiveness of the earth's magnetic shield in preventing sea-level cosmic showers is discussed in terms of the primary proton's "rigidity". We define a terrestrial geomagnetic rigidity, R_c as the minimum energy that a primary proton must have to create a cascade which can reach sea level at a specific geomagnetic point [Ziegler, 1996]. In [Störmer, 1955] is proposed a relation in order to compute R_c in the approximation of a dipole field:

$$R_c = \frac{\left[M \cos^4 \lambda\right]}{r^2 \left[1 + (1 - \sin \epsilon \sin \xi \cos^3 \lambda)^{1/2}\right]^2} \qquad (2.1)$$

Where M is the magnitude of the dipole moment, λ is the latitude from the magnetic equator, ϵ is the angle from the zenith direction, ξ the azimuthal angle measured clockwise from the direction to the north magnetic pole and r is the distance from the dipole centre. Another way is to determine R_c by numerical integration of backward trajectories in a model of the geomagnetic field as in [Ütikofer et al., 2007]. An example of results it is show in figure 2.5, as we expect we notice that R_c is greater at the equator and smaller at the poles.

12
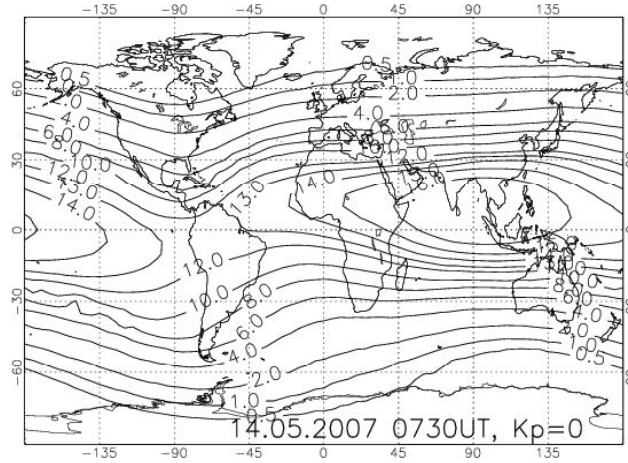
Figure 2.5: World map with computed geomagnetic vertical cut-off rigidity contour lines [Ütikofer et al., 2007]

On the other hand temporal variations in cosmic-ray intensity are due to solar activity. During a solar maximum, related to a maximum sunspot counts, the stronger solar magnetic field deflects a greater fraction of the galactic protons away from the Earth, and the galactic cosmic-ray intensity on Earth is reduced. Conversely, during low solar activity the weaker solar magnetic field not deflect to much galactic protons and the galactic cosmic-ray intensity on Earth is higher. Shorter-term fluctuations have a similar effect (albeit of smaller amplitude) on the cosmic-ray intensity. Changes in the shape of the geomagnetic field which occur on the time scales of years to decades are of secondary importance to temporal variations in the cosmic-ray intensity. A solar cycle lasts about 11 years. The alternation of maxima of sunspot number can be show in figure 2.6. The vertical red lines delimit the various cycle from 1951 to 2020. As we can see there is an anti correlation between the cosmic neutron counts and the sunspot counts, as we describe before.

The neutrons generated by primary cosmic-ray are high-energy neutrons. When they interact with atmosphere and soil they loose energy and some of them can reach thermal equilibrium. The energy spectrum of the neutron cosmic rays can vary from 1 GeV to 25 meV. The energy spectrum for neutrons at ground level is show in figure 2.7 , where the three peaks can be divided according to their energy:

- High-energetic neutrons, form 10 MeV to 1GeV (red region in figure 2.7). They are produced in collision between primary cosmic ray mainly oxygen and nitrogen nucleus. This collision produces a cascade of lighter particles, include neutrons. When cosmic rays enter the Earth's atmosphere they collide with atoms and molecules.

- Fast neutrons, with energy on the order of 1 MeV (green region in figure 2.7). They are generated by evaporation of exited air or soil nucleus, hit by high-energy neutrons or protons interact with air or soil.

- Epithermal and fast neutrons, with energy less than 1 MeV (blue region in figure
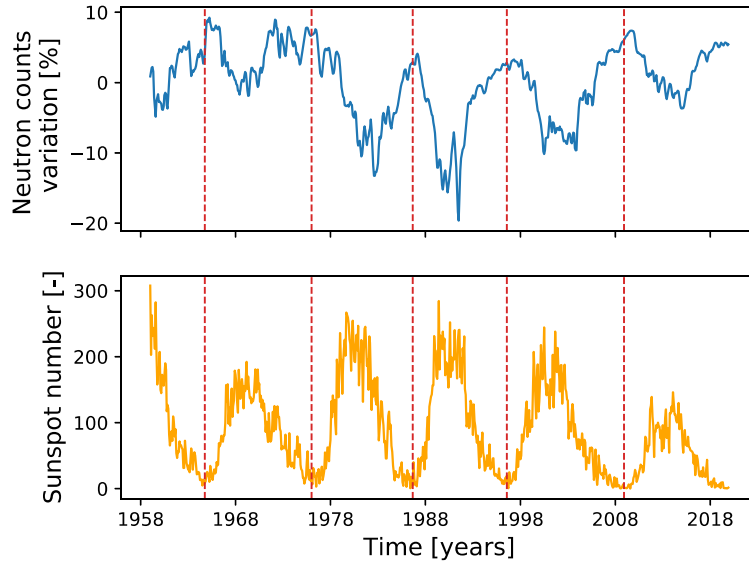
Figure 2.6: In 1st panel it is show the neutron count variation determine in IGY Jungfraujoch (Coord: 46.55N, 7.98E; Alt: 3570 m) [Source:`www.nmdb.eu/data`] and in the 2nd the sunspot number related to solar activity [Source:`www.sidc.be`]. The red line delimited the Sun cycle.
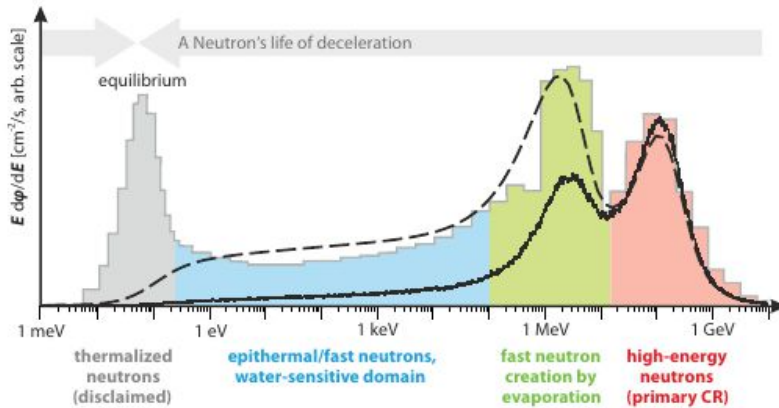
Figure 2.7: Neutron energy spectra at the surface: exemplary measurement and simulated (dashed) [Köhli et al., 2015].

2.7) are dominated by elastic collision. This energy band is most sensitive to water and organic molecules and thus most relevant for the CRNS method [Köhli et al., 2015].

- Termalized neutrons that have an energy of the order of $k_b T \approx 26$ meV. After multiple collision the energetic neutrons reach the thermal equilibrium. This region is the lower part of the spectrum (grey region in figure 2.7)

14

2.4 Interaction of neutrons with matter

Neutrons have zero charge, for this reason they can not interact with mater electromagnetically. In fact they can interact only via strong force. Above thermal energies, neutrons lose energy with elastic collision and cannot accelerate to higher energies due to their neutral electrical charge. For slow or thermal neutrons the main cause of their disappears is nuclear capture. In this section all the information that are reported are taken from [Knoll, 2010] and [Krane et al., 1987]

2.4.1 Fast neutrons moderation

The process of moderation (slowing or stopping) of neutrons depends on two factors that together define the neutron stopping power of a material:

  (a) the probability of scattering by different elements, characterized by their microscopic scattering cross-sections, and, in combination with the number of nuclei of different elements, or the elemental concentration, the resultant macroscopic scattering cross-section of the material

  (b) the energy loss per collision or, inversely, the number of collisions necessary to moderate a fast neutron

When a thickness dx of a material is crossing by a neutron, it will encounter ndx atom per unit surface area of the material, where n is the number of atoms per unit volume. If σ_t is the total cross section fo elastic neutron scattering, the intensity I decrease with absorber thickness according to an exponential relationship:

$$I = I_0 e^{-\sigma_t n x}. \tag{2.2}$$

The comparison of elastic neutron cross section for the nucleus most present in atmosphere and soil is show in figure 2.8.

With relation 2.2 we can determine the change in intensity of those with a initial energy. For determine the decrease in the total number of neutrons we must use a different approach. Let's consider an elastic collision, as in figure 2.9, between a neutron of initial energy E_n, with a target nucleus of mass A, and moreover we indicate with θ the scattering angle of the recoil nucleus in the lab coordinate system.

For incoming neutrons with non-relativistic kinetic energy ($E_n \ll 939 MeV$), conservation of momentum and energy in the centre of mass can be used in order to determine E_R in function of E_n. After that we can covert the result to the more familiar laboratory coordinate frame an we obtain the following relationship:
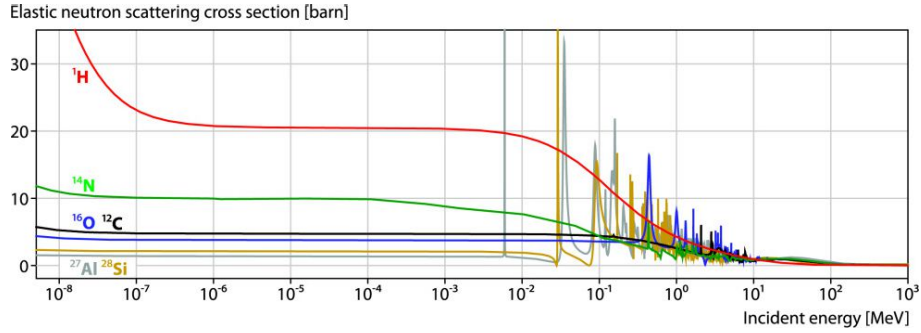
Figure 2.8: Comparison of elastic neutron cross sections of hydrogen (red), nitrogen (green), oxygen (blue), carbon (black), silicon (ocher), and aluminium (grey) for kinetic energies between 5 meV and 1000 MeV [Köhli et al., 2015]
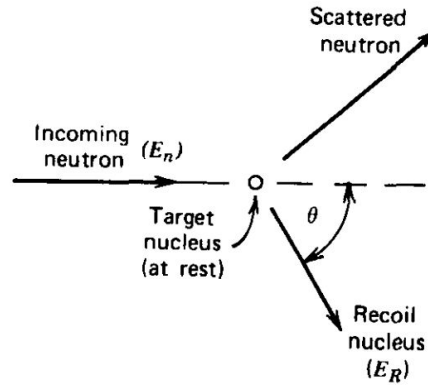
Figure 2.9: Neutron elastic scattering diagram for the laboratory coordinate system [Knoll, 2010]

$$E_R = \frac{4A}{(1+A)^2}(\cos\theta)^2 E_n \tag{2.3}$$

From equation 2.3 we can see that the energy given to the recoil nucleus is uniquely determined by the scattering angle. If we consider a head-on collision of the incoming neutron with the target nucleus will lead to a recoil in the same direction ($\theta \simeq 0$), resulting in the maximum possible recoil energy:

$$E_R|_{max} = \frac{4A}{(1+A)^2}E_n \tag{2.4}$$

In figure 2.10 are show the maximum fraction of the incoming neutron that can be transfer to a recoil nucleus in a single collision for a variety of target nuclei. As we can see that only in collision with hydrogen the neutron can transfer all its energy in a single encounter. This trend explain why it is possible to determine water (H_2O) content in the soil using energetic cosmic neutrons.

Now if we want to determine the average number of scattering that are needed to ther-
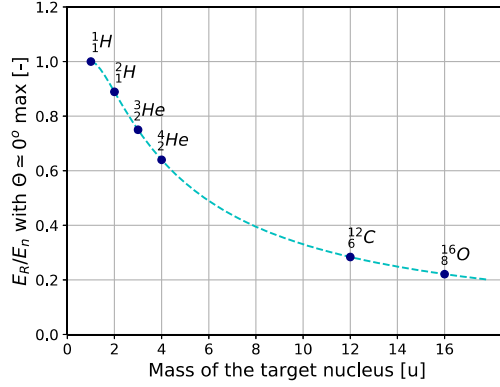
Figure 2.10: Maximum fractional energy transfer in neutron elastic scattering

malize a energetic neutron we can proceed as follow. We define the parameter ξ, that represent the average value of $log(\frac{E}{E'})$ after a single collision, where E and E' represent neutron energy before and after the scattering. From this definition we can write:

$$\xi = \left[\ln \frac{E}{E'}\right]_{av} = \frac{\int \frac{(A+1)^2}{A^2+1+2A\cos\theta} d\Omega}{\int d\Omega} \tag{2.5}$$

Where $d\Omega$ is the element of solid angle in the centre of mass system. Here again we assume the scattering to be isotropic. Carrying out the integration gives the relation 2.6

$$\xi = 1 + \frac{(A-1)^2}{2A}\ln\left(\frac{A-1}{A+1}\right) \tag{2.6}$$

Finally we can found a relation (2.7) that give us the number of interaction, n, that are need to pass from a energetic neutron of energy E to a thermal neutron of energy E_T.

$$n = -\frac{1}{\xi}\ln\left(\frac{E}{E_T}\right) \tag{2.7}$$

In table 2.1 are reported the moderating property of some nuclei. We can see that the best performance are achieved using hydrogen as moderator.

Nucleus	ξ	n (for thermalization)
^{1}H	1.00	18
^{2}H	0.725	25
^{4}He	0.425	43
^{12}C	0.158	110
^{208}Pb	0.0096	1895

Table 2.1: Moderating proprieties of various nuclei, with $E_n \sim 2\text{MeV}$

2.4.2   Inelastic scattering

Inelastic scattering is similar to elastic scattering except that the nucleus undergoes an internal rearrangement into an excited state from which it eventually releases radiation. The total kinetic energy of the outgoing neutron and nucleus is less than the kinetic energy of the incoming neutron; part of the original kinetic energy is used to place the nucleus into the excited state. It is no easy to write an expression for the average energy loss because it depends on the energy levels within the nucleus. But the net effect on the neutron is again to reduce its speed and change its direction. If all the excited states of the nucleus are too high in energy to be reached with the energy available from the incoming neutron, inelastic scattering is impossible. In particular, the hydrogen nucleus does not have excited state so only elastic scattering can occur in that case. In general, scattering moderates or reduces the energy of neutrons and provides the basis for some neutron detectors (for example, proton recoil detectors).

2.4.3   Neutron absorption

Instead of being scattered by a nucleus, the neutron can be absorbed or captured. The nucleus may rearrange its internal structure and release one or more gamma rays. Charged particles can also be emitted, the more common ones are protons, deuterons, and alpha particles. The emission of only one neutron is indistinguishable from a scattering event. If more than one neutron is emitted, the number of neutrons now moving through the material is larger than the number present before the interaction; the number is said to have been multiplied.

2.5   Correction for neutron counts

As discuss in section 2.3 the cosmic neutron flux is not constant in space and time [Desilets and Zreda, 2003]. The quantity that can modify the neutron flux and the relative correction factors are the following:

- Variation of the incoming cosmic ray flux due to astronomical events, f_I

- Atmospheric water vapour, f_W

- Atmospheric pressure variation, f_P

So at the end neutron rate that we acquire with the detector must be corrected as reported in equation 2.8 [Zreda et al., 2008].

$$N_{corr} = N_{raw} \cdot f_I \cdot f_W \cdot f_P \tag{2.8}$$

In the following section we describe how to determine these correction coefficients.

2.5.1 Correction due to variation of incoming cosmic ray flux

As discuss in section 2.3, the neutron cosmic ray flux is influenced by the solar activity. For this reason we must introduce a correction factor f_I, define as:

$$f_I = \frac{I_M}{I_0} \tag{2.9}$$

Where f_I is merely the ratio of the measured neutron monitor intensity, I_M, at a given time to a specified baseline reference intensity, I_0. The value I_0 can be found in the "Real-Time Database for high-resolution Neutron Monitor measurements". It provides access to neutron monitor measurements from stations around the world.

2.5.2 Pressure correction

When the neutrons are generated in the atmosphere they pass through several kilometer of atmosphere, so the initial flux decrease in exponential way. The pressure correction parameter f_P is given by

$$f_P = \exp\left(\frac{P - P_0}{L}\right) = \exp(\beta(P - P_0)) \tag{2.10}$$

where L is the mass attenuation length for high-energy neutrons (mbar or equivalent in g/cm^2) that varies progressively between $\sim$128 g/cm^2 at high latitudes and ~ 142 g/cm^2 at the equator [Desilets and Zreda, 2003]. Alternatively can be use its reciprocal, $\beta = \frac{1}{L}$, the attenuation coefficient, also called barometric factor. P is the pressure at the specific site, and P_0 is an arbitrary reference pressure (which can be selected to be the long-term average pressure at the specific site, sea-level pressure, or long-term average pressure at a different reference site).

2.5.3 Water vapour correction

The water vapour correction is discuss in [Rosolem et al., 2013], in this paper they use "Monte Carlo N-Particle Transport Code" in order to found a the correction parameter f_W. They obtain the following relation:

$$f_W = 1 + 0.0054 \cdot \Delta\rho_{v0} \tag{2.11}$$
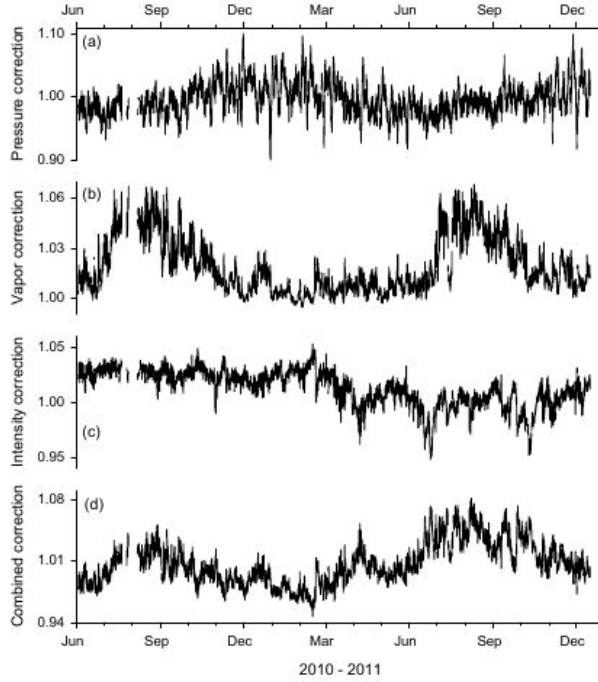
Figure 2.11: Fast neutron intensity was corrected with: panel (a) atmospheric pressure, panel (b) atmospheric water vapour and in panel (c) for temporal changes in the incoming neutron intensity. In panel (d) the fast neutron was corrected with all of them [Zreda et al., 2012]

where $\Delta\rho_{v0} = \rho_{v0} - \rho_{v0}^{ref}$ is the difference in the absolute humidity at the time of measurement (ρ_{v0}) and at the reference time (ρ_{v0}^{ref}), for example that at the time of calibration, all measured at the surface in g/m^3.

The impact of the three correction parameter is show in figure 2.11. As we can see pressure variations have the largest effect on the neutron intensity, with the correction factor ranging from 0.9 to 1.1 and a small seasonal effect. Water vapour correction displays larger seasonality, but a smaller range from 0.99 to 1.07. The intensity correction ranges from 0.95 to 1.05 and has no seasonal trend. Due to cancelling effect, the combined correction has a smaller magnitude than the pressure correction, and ranges from 0.95 to 1.08.

2.6   Calibration of CRNS

The fast neutron rate can be convert in soil moisture with an empirical formula reported in [Desilets et al., 2010]. The relation is the following:

$$\theta(N) = \frac{a_0}{\left(\frac{N}{N_0}\right) - a_1} - a_2 \tag{2.12}$$

where θ is the gravimetric water content (kg/kg), N is the neutron counting rate normalized to a reference atmospheric pressure and solar activity level, N_0 is the counting rate over dry soil under the same reference conditions; a_i are fitting parameters, the values proposed in [Desilets et al., 2010] are:

$$\begin{cases} a_0 = 0.0808 \\ a_1 = 0.372 \\ a_2 = 0.115 \end{cases} \tag{2.13}$$

These parameters were determined for a generic silica soil matrix [Desilets et al., 2010]. Excellent agreement between water contents calculated with this equation and those measured gravimetrically in field samples at Lewis Springs, Arizona (2.12) suggest that model calibration parameters are widely applicable to soils derived from silicate rocks. As noted by [Desilets et al., 2010], the equation works only for moisture levels greater than 0.02 kg/kg, but because of water in mineral lattices and in organic matter that is present in most soils, the equation should be applicable to most soils.
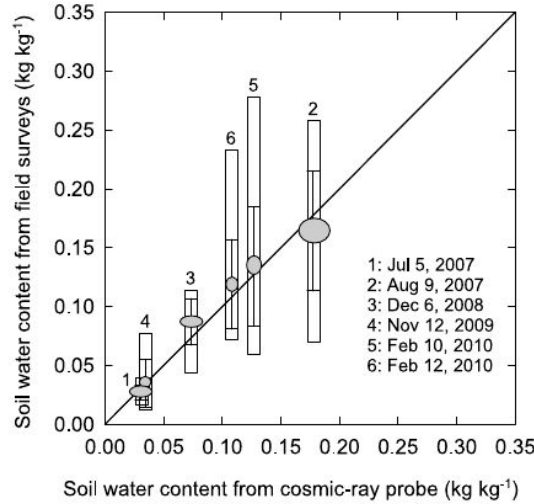
Figure 2.12: Water content at Lewis Springs, Arizona, determined from the cosmic ray probe using equation 2.12 compared against averages of spatially distributed depth profiles collected in field surveys. Counting rates are corrected for variations in barometric pressure and solar activity. The vertical component of the error ellipse represents the standard error of the mean for depth-averaged samples taken in manual soil surveys. The horizontal component represents the standard error in the moisture determination propagated from the statistical uncertainty in the counting rate. Error bars give the standard deviation of the depth-averaged samples, while the vertical rectangles encompass the entire range of depth-averaged samples [Desilets et al., 2010].

More recently, in [Baroni et al., 2018] the equation was adjusted to account for additional hydrogen pools. These changes result in the following modified equation:

$$\theta_{CRNS} = \theta_{T(wt)} = \left(\frac{a_0}{\frac{N_c}{N_0} - a_1} - a_2 \right) \frac{\rho_b}{\rho_w} \quad \text{with} \quad \theta_{T(wt)} = (\theta_v + LW + W_{SOC})_{wt} \quad (2.14)$$

where θ_{CRNS} is volumetric water content estimated by CRNS (m^3/m^3), the parameters a_i are the same reported in 2.13; ρ_b and ρ_w are the soil bulk density (g/cm^3) and density of water (assumed to be 1 g/cm^3), respectively. The main differences respect to equation 2.12 is that θ_{CRNS} is the sum of three different term, θ_v, LW and W_{SOC}. So at the end for the correct determination of θ_v from equation 2.14 we must subtract the LW and W_{SOC} contributions.

2.7 Measurement volume

2.7.1 Measurement area

The measurement area, also called horizontal footprint of a geophysical instrument generally covers the area in which the medium of interest is probed and the carrier of such information is detected. The scenario of a centrally located sensor which detects neutrons isotropically exhibits point symmetry and thus leads to the assumption of a circular footprint area, $A = r^2\pi$. By assuming an exponential decay of detected neutron intensity over travel distance, in [Zreda et al., 2012] the horizontal footprint is defined as the area around the probe from which $(1 - \exp^{-2})$, equal to 86%, of counted neutrons arise. The number of neutrons N_R that have originated within a distance R from the sensor is given by:

$$N_R = \int_0^R W_r dr \qquad (2.15)$$

Where W_R is the radial weighting function. In order to find the distance within which 86% of the detected neutrons originate, the following equation is solved for R_{86} numerically:

$$\int_0^{R_{86}} W_r dr = 0.86 \int_0^{\infty} W_r dr \qquad (2.16)$$

In [Köhli et al., 2015] are reported the radial decrease of the detected neutron intensity W_R from a Monte Carlo simulations. The main result are show in figure 2.13. In the simulation is set a variety of volumetric water contents in the soil from 0% to 50% and absolute humidity in the air from 0 to 50 g/m^3. Wr can assist in finding a properly weighted mean of independent soil moisture measurements. It further shows that little contribution is made by neutrons from r>200 m and highest contribution comes from r<10 m around the sensor.
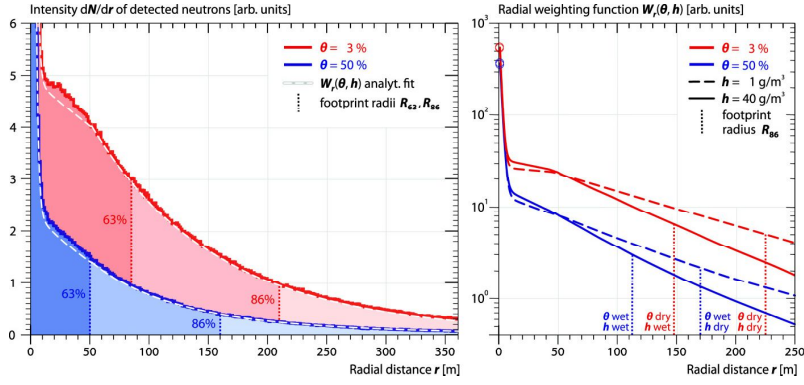
Figure 2.13: Detected neutron intensity dN/dr over distance r between origin and detection (right). Radial weighting function W_r from simulation (left). Simulations were performed for humidity h=10 g/m^3 and two exemplary soil moistures θ=3% and 50%. [Köhli et al., 2015]

The peak at r<10 m accounts for neutrons that directly emerge from the ground and have a high probability to be detected even though most of them come from the lower part of the neutron energy spectrum. The region up to r<50 m describes the average mean free path of most of the environmental neutrons in humid air. For distances between 50 and 200 m, neutrons interact with the soil multiple times until they are detected, which in turn means that with increasing r, average neutron energies quickly become insufficient in order to arrive at the detector before thermalization. From about 200 m on, detected neutrons are dominated by the higher energetic part of the spectrum, which appear to be higher in flux rates and are able to probe the soil very far from the detector.

Due to the different neutron energies involved, [Köhli et al., 2015] found an accurate fit to the intensity distribution, show in figure 2.13, by splitting the radial domain into four exponential parts. An analytical description can be obtained for $\theta > 2\%$:

$$W_r(h, \theta) \approx \begin{cases} F_1 \exp^{-F_2 r} + F_3 \exp^{-F_4 r}, & \text{for} \quad 0.5 < r \leq 50\text{m} \\ F_5 \exp^{-F_6 r} + F_7 \exp^{-F_8 r}, & \text{for} \quad 50 < r < 600\text{m} \end{cases} \qquad (2.17)$$

where the parameter functions F_i are individually dependent on humidity and soil moisture. From this definition of W_r and using equation 2.16 we can find R_{68}. The numerical result are show in figure 2.14.

The footprint radius R_{86} that we found before is influence by the presence of vegetation and air pressure. From the perspective of the neutron, the layer of height H_{veg} introduces by vegetation is a new source of hydrogen in the air and consequently reduces the travelling range in the same manner as humidity. On the other hand, the footprint can expand with decreasing air pressure (e.g., increasing altitude). The lower air density allows neutrons to cover longer distances between collisions. For this reason by taking the scaling factors into account, the final footprint radius can be estimated with:
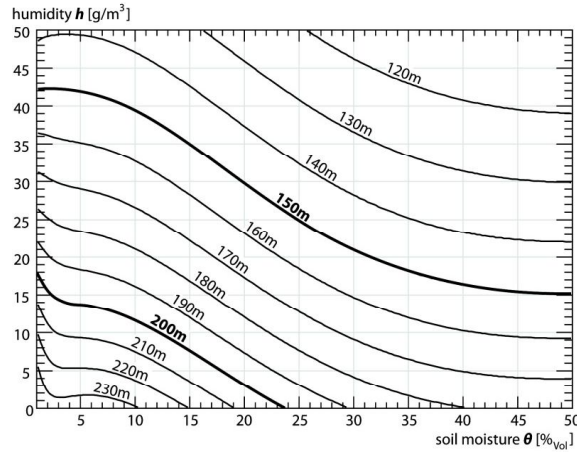
Figure 2.14: Footprint radius R_{86} (contour lines) and its dependency on soil moisture θ and air humidity h at sea level. [Köhli et al., 2015]

$$R_{86}(h, \theta, p, \text{veg}) = f_P \cdot f_{veg}(\theta) \cdot R_{86}(h, \theta) \tag{2.18}$$

where f_P and f_{veg} are the correction for atmospheric pressure and vegetation respectively. The value of this parameter are show in figure 2.15.
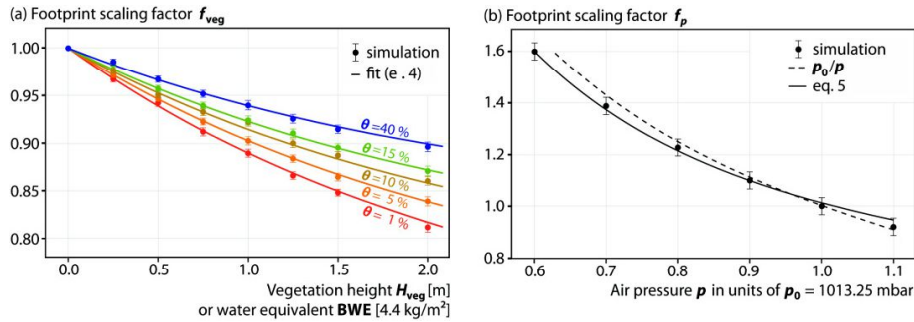
Figure 2.15: Change of the footprint radius $R_{86}(h, \theta)$ by vegetation and air pressure. The scaling factor f_{veg} is reduced by vegetation height which corresponds to a biomass water equivalent. [Köhli et al., 2015]

2.7.2   Measurement depth

The thickness of the probed soil layer is an important advantage of the CRNS method compared to most remote-sensing products. Cosmic-ray neutrons can penetrate the first decimetres of the soil, whereas electromagnetic signals interact within the upper 0–5 cm. The effective depth of measurement, which is defined as the thickness of soil from which 86% of counted neutrons arise, like in the footprint radius, depends strongly on soil moisture [Zreda et al., 2008]. In [Köhli et al., 2015] a simple analytical description of the vertical weighting function was reported for $\theta \geq 10\%$:
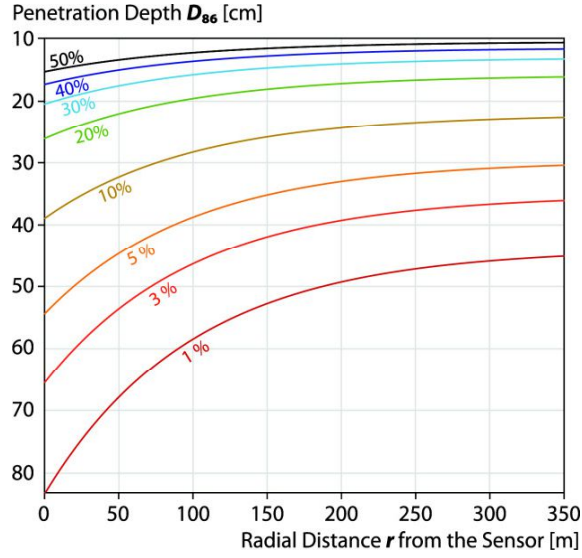
Figure 2.16: Dependency of the penetration depth D_{86} on radial distance r to the sensor for a range of soil water contents θ (colored). [Köhli et al., 2015]

$$W_d(r,\theta) \propto \exp\left(-\frac{2d}{D_{86}(r,\theta)}\right) \qquad (2.19)$$

The relation can be used to obtain a properly averaged mean value of point measurements. Figure 2.16 shows penetration depths $D_{86}(r,\theta)$ as a function of radial distance r from the sensor for exemplary soil moisture values θ. For dry soil, $D_{86}(r,\theta \approx 1\%)$ ranges from 83 cm right below the sensor to 46 cm at r=300 m distance. The penetration depth varies between 15 cm and 83 cm below the sensor for wet and dry soil, respectively.

At the end we can conclude that the horizontal footprint is of the order of 10^2 m and in the vertical depth from 10 to 100 cm. These value are of the order of magnitude that are important for soil moisture estimation in precision agriculture.

2.8 Biomass estimation with CRNS

CRNS measurement is not only sensitive to soil water content (SWC) but also influenced by hydrogen stored in other pools, such as biomass, litter, snow, and canopy interception [Desilets et al., 2010]. For this reason [Tian et al., 2016b] proposed to use the ratio of thermal to fast neutron intensity measured with the CRNS probe to estimate aboveground biomass for maize and soybean crops. In [Jakobi et al., 2018] is reported that it would be highly attractive to estimate biomass directly using CRNS for at least two reasons. First, it would allow to remove effects of time-varying biomass from SWC estimates obtained with CRNS without the need for additional measurements. Second, simultaneous measurements of SWC and biomass dynamics at the field scale would be very useful to im-

prove the understanding of relationships between plant growth and SWC deficit, which is essential for the development of adaptation strategies against drought-induced restrictions in crop production [Jakobi et al., 2018]. Total biomass water equivalent (BWE) consists of vegetation water as well as hydrogen present in the biomass tissue. A comparison of BWE estimated from the neutron rate (N_r) and measured BWE a is provided in figure 2.17
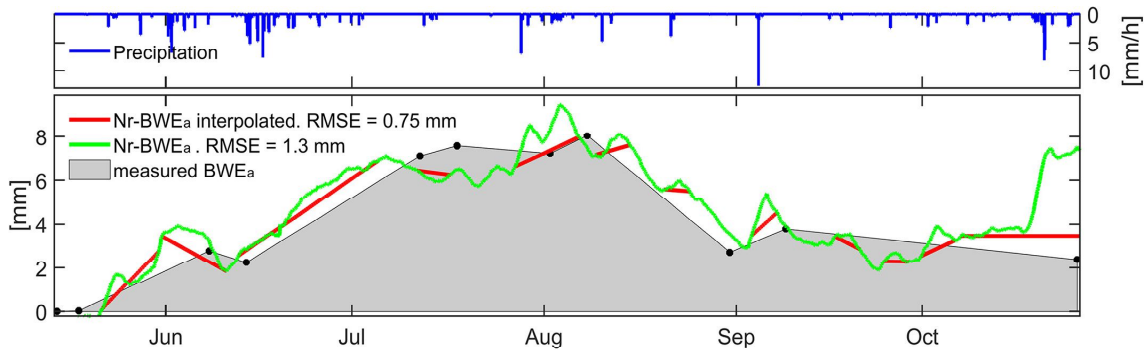
Figure 2.17: Time series of measured (grey area) and N_r-derived (green) BWE. The red line indicates an interpolated time series of N_r-derived BWE where data points were removed that occurred within 3 days after a 24-hr period with precipitation $\geq$ 1.5 mm. The observed increases in Nr-BWEa before the respective precipitation events are explained by the use of a 3-day moving average. RMSE = root-mean-square error [Jakobi et al., 2018]

Chapter 3

Instrumental apparatus

In the previous section we describe the CRNS tecnicque proposed by [Desilets and Zreda, 2003]. In the first part of this chapter we breafly report the detector used in COsmic-ray Soil Moisture Observing System (COSMOS) [Zreda et al., 2012] and after we describe in detail the novel apparatus, called FINAPP, that we developed at University of Padova.

3.1 COSMOS probe

In [Zreda et al., 2012] for neutron counting they used a gas-filled counter. This detectors comprise a metal tube filled with gas enriched with ^{3}He that reacts with thermal neutrons that enter the tube through the reaction

$$^3_2He +^1_0 n \rightarrow^3_1 H +^1_1 p \qquad Q_{value} = 0.764 MeV \tag{3.1}$$
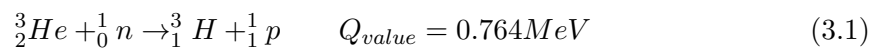
As we can see neutron absorption reaction results in the emission of charged particles, creating ionization in the tube, which results in an electronic pulse that can be read by charge-sensitive electronics. A potential of $\sim$1 kV is applied between the tube wall (the cathode) and a thin central wire (the anode). When a thermal neutron collides with an atom of the enriched gas, the resulting ionization produces a cascade of electrons, called a Townsend avalanche. These electrons are attracted to the anode and produce a charge pulse. This pulse is amplified and at the end we obtain an electronic signal that can be acquire by a data acquisition [Knoll, 2010]. A pictorial representation of the detector is show in figure 3.1.

The main disadvantage of this detector is due to the fact that is very difficult to obtain ^{3}He because the sole method currently used to produce this inert gas is simply collecting it as a by product from the radioactive decay of tritium:
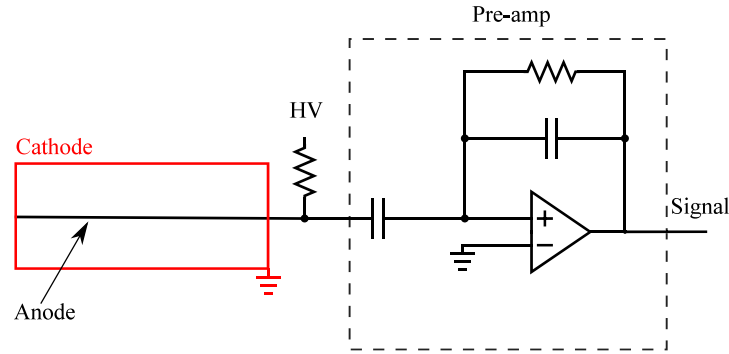
**Figure 3.1:** The geometry of a cylindrical proportional counter

$$^3_1He \rightarrow^3_1 H + e^- + \overline{\nu_e} \qquad t_{1/2} = 12.3y \qquad (3.2)$$
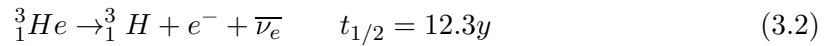
Stores of tritium must occasionally be processed to remove the ingrown ^{3}He and maintain the desired tritium concentration. This tritium comes from the refurbishment and dismantlement of the nuclear stockpile. The production of ^{3}He from tritium decay has declined as the nuclear weapons stockpile has been reduced. However, the demand for ^{3}He based neutron detectors used to support homeland security objectives has increased significantly. The reduced production and increased demand has resulted in a significant shortage of ^{3}He [Kouzes, 2009]. For this reason in the FINAPP setup we substitute the ^{3}He counter with other detector type.

3.2 FINAPP apparatus

FINAPP apparatus is composed by the following part:

- Two detectors, one for the neutrons, the other for the muon detection that are used for study the incoming cosmic ray flux

- two photomultipliers used for the conversion of the scintillation photons intro electric signal

- electronics for the signal acquisition and data storage

- weather sensor composed by thermometer, barometer and hygrometer

In figure 3.2 is show the scheme of the detection system.
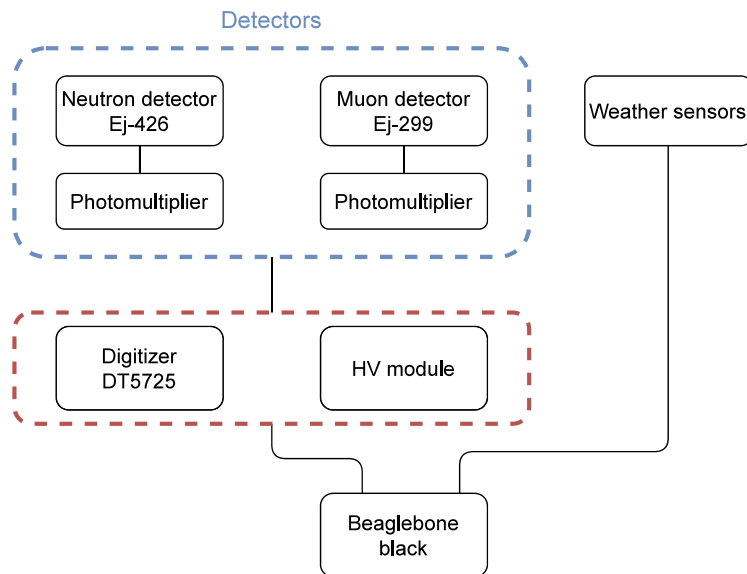
Figure 3.2: Block scheme detection system.

3.2.1 Detectors

In the FINAPP apparatus we use scintillator detectors. They are made of some particular materials that are able to emits light when they are hit by radiations. The ideal scintillation material should possess the following properties [Knoll, 2010]:

- It should convert the kinetic energy of charged particles into detectable light with a high scintillation efficiency.

- The light yield should be proportional to deposited energy over as wide a range as possible.

- The medium should be transparent to the wavelength of its own emission for good light collection.

- The decay time of the induced luminescence should be short so that fast signal pulses can be generated

- The material should be of good optical quality and subject to manufacture in sizes large enough to be of interest as a practical detector

- Its index of refraction should be near that of glass to permit efficient coupling of the scintillation light to a photomultiplier tube or other light sensor

No material simultaneously meets all these criteria, and the choice of a particular scintillator is always a compromise among these and other factors. In our we decide to use two different scintillators. An inorganic scintillator (Ej-426) for the neutron detection and an

organic scintillator (Ej-299 and Ej-309) for gamma and muon detection.

Neutron detector

For neutron detection we decide to substitute the ^{3}He proportional counter with an in-organic scintillator (Ej-426). The main advantage of this type of detector is that made of material that are easier to find, respect ^{3}He and it is safer from a security point of view respect a liquid scintillator (i.e. Ej-309). Ej-426 is an efficient detector for thermal neutrons with low sensitivity to gamma radiation. The detector has the form of a flat, white, thin sheet (see figure 3.3a), consisting of a homogeneous matrix of fine particles of lithium-6-fluoride (^{6}LiF) and zinc sulfide phosphor (ZnS:Ag) compactly dispersed in a colourless binder.

(a) *Ej-426 sheet*

(b) *Ej-426 emission spectrum*
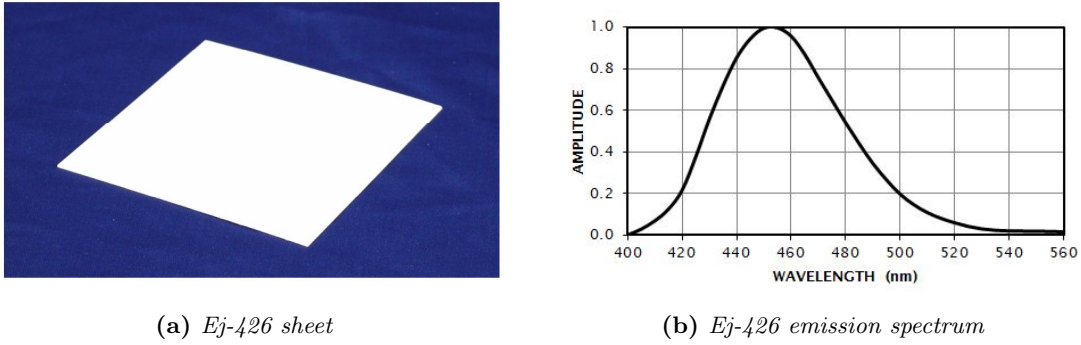
Figure 3.3: Thermal neutron detector Ej-426

The neutron detection process employs the nuclear reaction ^{6}Li(n,α)^{3}H:

$$^6Li + n \rightarrow^3 H +^4 He + 4.78 MeV \tag{3.3}$$

with a cross section of 941 barns for 0.025 eV neutrons. The resulting triton and alpha particle are detected by ZnS:Ag phosphor with the broad blue fluorescent spectrum shown in figure 3.3b. The main properties of the detector are reported in table 3.1.

Propriety	Value
Dimension	15 x 15 cm
Thickness	0.51mm
^{6}LiF:ZnS Mass Ratio	1:3
^{6}Li Density (atoms/cm3)	$8.81 \cdot 10^{21}$
Theoretical N^{TH} Efficiency	0.31

Table 3.1: Propriety of Ej-426 detector [Source:`www.eljentechnology.com`]

Scintillation mechanism in inorganic scintillator   The scintillation mechanism in inorganic materials depends on the energy states determined by the crystal lattice of the material. As shown in figure 3.4, electrons have available only discrete bands of energy in materials classified as insulators or semiconductors.
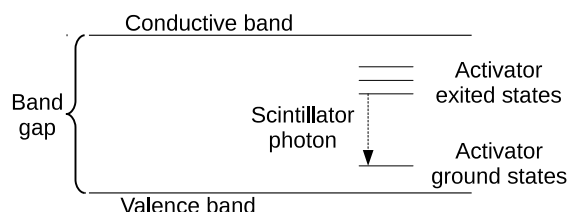

Figure 3.4: Energy band structure of an activated crystalline scintillator [Knoll, 2010]

The lower band, called the valence band, represents those electrons that are essentially bound at lattice sites, whereas the conduction band represents those electrons that have sufficient energy to be free to migrate throughout the crystal. There exists an intermediate band of energies, called the forbidden band, in which electrons can never be found in the pure crystal. Absorption of energy can result in the elevation of an electron from in the valence band across the gap into the conduction band, leaving a hole in the normally filled valence band. In the pure crystal, the return of the electron to the valence band with the emission of a photon is an inefficient process. Furthermore, typical gap widths are such that the resulting photon would be of too high an energy to lie in the visible range. To enhance the probability of visible photon emission during the de-excitation process, small amounts of an impurity are commonly added to inorganic scintillators. Such deliberately added impurities, called activators, create special sites in the lattice at which the normal energy band structure is modified from that of the pure crystal. As a result, there will be energy states created within the forbidden gap through which the electron can de-excite back to the valence band. Because the energy is less than that of the full forbidden gap, this transition can now give rise to a visible photon and therefore serve as the basis of the scintillation process. A charged particle, in our case α particle, passing through the detection medium will form a large number of electron-hole pairs created by the elevation of electrons from the valence to the conduction band, consequently there are the formation of a large number of scintillation photons [Knoll, 2010].

Once we have the light signal we must collect them and send it to the photomultiplier (PMT) in order to generate an electric signal. The direct matching of the (PMT) to the scintillator is impossible due to the large dimension of the Ej-426 sheet. For this reason we put on the scintillator a wavelength shifter (WLS) plastics Ej-280 that are able to absorb and shifting the emission spectra of Ej-426. The WLS is directly connected to the PMT. In table 3.1 is reported the theoretical efficiency of neutron detection that is of the order of 31%. For our experiment we need an higher efficiency, for this reason we use 3 Ej-426 sheet coupled with two WLS Ej-280. We call this detector configuration Finapp3.

A picture of Finapp3 is show in figure 3.5.

(a)   (b)
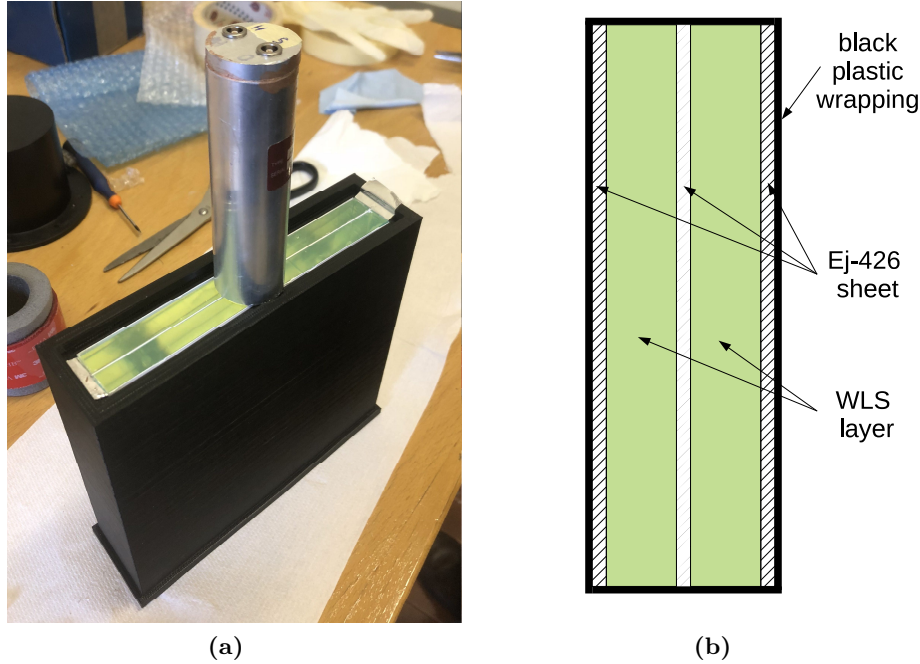
Figure 3.5: Picture of the neutron detector with the PMT (3.5a). Draw (not in scale) of horizontal section of the detector, it is possible to see the three different Ej-426 sheet match with the two WLS layer (3.5b).

As discuss in chapter 2 we are interested in fast neutron rate, while this detector are able to reveal only thermal neutrons. For this reason we put a polyethylene shield around the detector in order to thermalize the fast neutron. In additional we put a gadolinium shield, outside the polyethylene, to stop the neutrons that are already thermalized. In fact thank to his cross section for thermal neutron capture ($2.5 \cdot 10^5$ b in ^{157}Gd, 15.7% abundant in natural gadolinium) this shield is able to stop most of thermal neutrons.

This detector is not only sensitive to neutrons but also to gamma radiation. For this reason in the first part of the thesis work I developed an algorithm that are able to select the neutron signal from other events. The algorithm is describe in detail in section 3.4.

Incoming flux detector

For the study of the incoming cosmic ray flux we focus our attention in the muon component. For this reason near the neutron detector we put a plastic scintillator Ej-299 or in other case Ej-309. In figure 3.6 and table 3.2 are reported the scintillator main characteristic.

These detectors are able to detect muons because muons are charged particle and ionize directly the organic materials. Moreover they are able to detect gamma rays. The

(a) *Ej-299 detector*

(b) *Ej-299 emission spectrum*
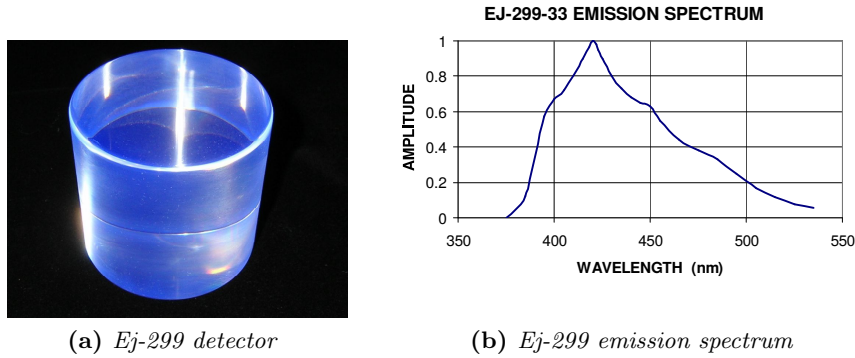
Figure 3.6: Ej-299 plastic scintillator

Propriety	Value
Dimension	cylinder of 7.62 x 7.62 cm
Light Output, % Anthracene	56
Scintillation Efficiency, photons/1 MeV e-	8600
Wavelength of Max. Emission	425 nm

Table 3.2: Propriety of Ej-426 detector [Source:`www.eljentechnology.com`]

gamma-rays come from the environmental radioactivity (i.e. ^{40}K). Due to the fact that the scintillator are made of atom with low Z (i.e. Hydrogen and Carbon) Compton scattering dominates in the interaction of the gamma rays with the detector, as show in figure 3.7.
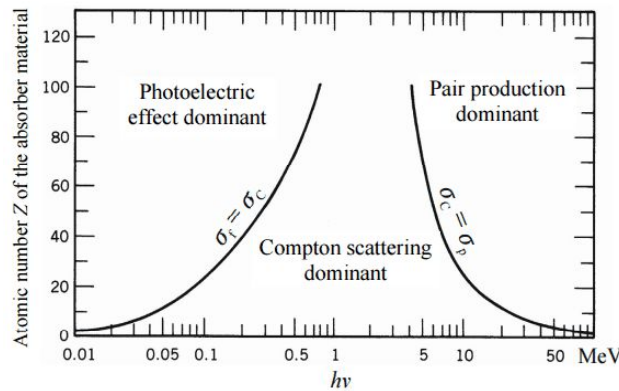
Figure 3.7: The relative importance of the three major types of gamma-ray interaction [Knoll, 2010]

The energy spectrum that we expected has a Compton-edge made by the ^{40}K gamma ray, that we use for the gain stabilization and a structure at higher energy made by cosmic muons.

Scintillation mechanism in organic scintillator   The fluorescence process in organics scintillator arises from transitions, induced by radiation, in the energy level structure of a single molecule and therefore can be observed from a given molecular species independent of its physical state.
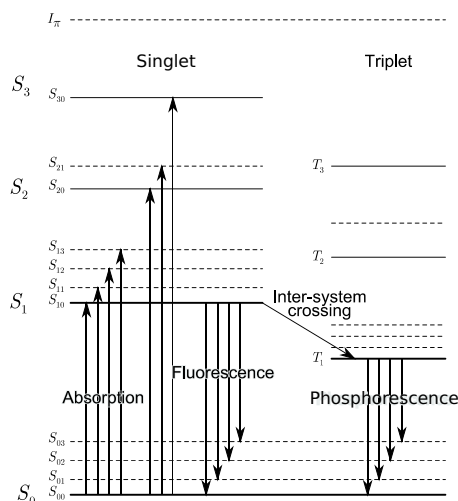
**Figure 3.8:** Energy levels of an organic molecule [Knoll, 2010]

In figure 3.8 the absorption of energy by the molecule is represented by the arrows pointing upward. In the case of a scintillator, these processes represent the absorption of kinetic energy from a charged particle passing nearby. The principal scintillation light (or prompt fluorescence) is emitted in transitions between singlet state and one of the vibrational states of the ground electronic state. The fluorescence decay time is of the order of few nanoseconds. Through a transition called inter-system crossing, some excited singlet states may be converted into triplet states. The lifetime of this T_1 may be as much as 10^{-3} the radiation emitted in a de-excitation from T_1 to S_0 is therefore a delayed light emission characterized as phosphorescence. Because T_1 lies below S_1, the wavelength of this phosphorescence spectrum will be longer than that for the fluorescence spectrum. While in the T_1 state, some molecules may be thermally excited back to the S_1 state and subsequently decay through normal fluorescence. This process represents the origin of the delayed fluorescence sometimes observed for organics.

3.2.2 Photomultiplier

In order to be convert the light from a scintillator into electrical signal we use a photomultiplier tube (PMT). A photomultiplier tube is a vacuum tube consisting of an input window, a photocathode, focusing electrodes, an electron multiplier (dynodes), and an anode sealed usually into an evacuated glass tube. Figure 3.9 shows the schematic construction of a photomultiplier tube.

In our experiment we use a Hamamatsu PMT mod. H6553. The PMT is powered by an

HV module CAEN mod. A7505. The module is a compact high efficiency power supply providing a programmable and monitorable output voltage ranging from 0 to 1600 V, when supplied with a +12 V input.
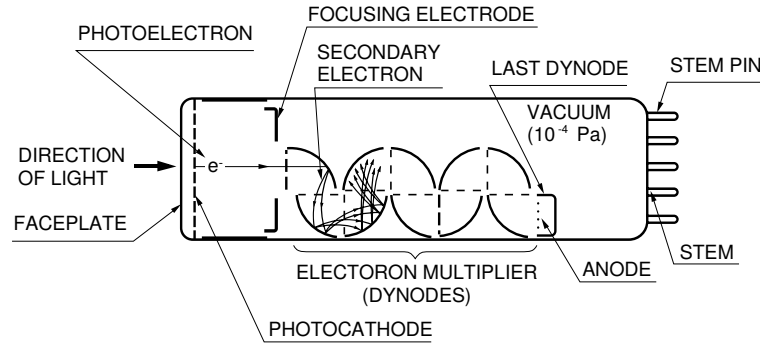
Figure 3.9: Basic element of a PMT [from:`www.hamamatsu.com`]

3.2.3   Data acquisition

The last block of the apparatus is formed by the data acquisition (DAQ) module, that is composed by a digitizer and a single board computer. The two components are show in figure 3.10.
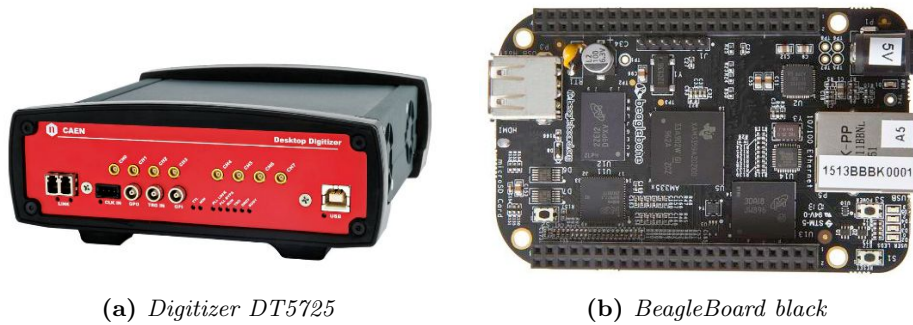
(a) *Digitizer DT5725*   **(b)** *BeagleBoard black*

Figure 3.10: Data acquisition module

The Desktop digitizer DT5725 is a CAEN Waveform Digitizer able to perform basic waveform recording and run online advanced algorithms (DPP) for digital pulse processing. The main characteristic are reported in table 3.3.

The digitizer receive and convert the analog signal intro digital signal and save it in a circular buffer. When the signal over pass a predefine value, called threshold, the trigger condition is verify and at this point the digitizer stop to acquire data. This signal can be directly send to the data storage or can be pre-processed. For do that several parameter can be set in the digitizer in order to determine the main parameter of the signal. For

Property	Value
Channels	8 channels single ended
Sampling rate	250 MS/s
Vertical resolution	14bit
Full Scale Range	0.5 or 2 V_{pp}
Communication interface	USB 2.0 compliant Transfer rate up to 30 MB/s

Table 3.3: Technical Specifications of CAEN Digitizer DT5725

example the integration gate for the determination of the signal energy. In figure 3.11 are show some gate that can be set.
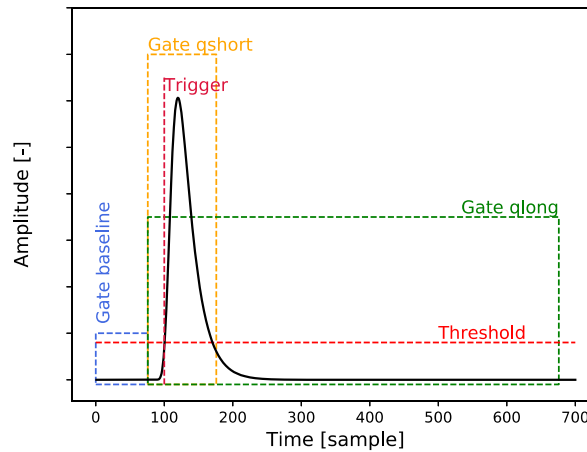
Figure 3.11: Example of signal (black line), polarity reversed, with the indication of the threshold and gate that can used in the pre-analysis

This second approach reduces the amount of data that needs to be stored. Each event is associated with a timestamp that equals the number of sample units since the acquisition was started. The data are send through USB cable to a BeagleBone black, that is a low-power open-source single-board computer. The specifications of the BeagleBone is reported in table 3.4

| Property	Value
Processor	AM335x 1GHz ARMⓇ Cortex-A8
RAM	512MB DDR3
Storage	64Gb
Operating system	Linux

Table 3.4: Technical Specifications of BeagleBone black

The software that controlling the data acquisition is ABCD, that is an open-source, dis-

tributed data acquisition system for nuclear detectors.

3.3   A distributed data acquisition system

The main characteristics of ABCD software is that is non a monolithic processes that run on a computer attached to the DAQ hardware (e.g. CAEN, MC2 Analyzer or ORTEC Maestro) but it is a fully distributed approach, in which all the tasks related to the DAQ are split over different processes. The interprocess communication is obtained through network sockets (or server) [Fontana et al., 2018]. The main advantage of this novel approach is that it is easier to isolate, test, and debug each part. In the figure 3.12 there is an example of DAQ architecture with independent module.
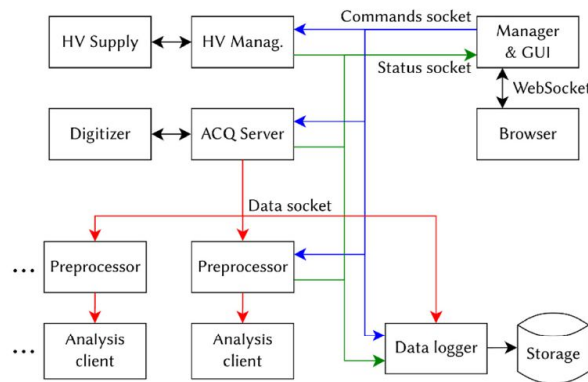
Figure 3.12: Example of DAQ architecture. Every box correspond to an independent module and the arrow represent the connection between the module [Fontana et al., 2018].

The communication between different module is implemented through ZeroMQ messaging library. The ZeroMQ library allows communication through dedicated virtual sockets. In ABCD there is a publish–subscribe (PUB–SUB) pattern for data and status streams, and a push–pull pattern for command delivery. The PUB–SUB pattern allows multiple subscriber clients to be connected to a single publisher server as show in figure 3.13.

All the processes statuses and raw data are published through a PUB socket, as this information can be used by many consumers. For example a module that are devoted to data analysis can subscribe to a PUB socket that publish the digitalized waveform.
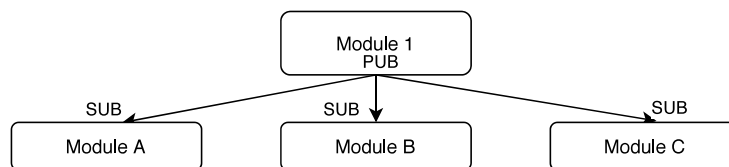
Figure 3.13: PUB–SUB pattern example

3.3.1   ABCD structure for data acquisition

As describe before ABCD is a modular software. Some module are devoted to the manage of the digitizer or the manage of the HV voltage. We focus our attention on the module dedicated to data acquisition.

In our case for every single events the digitizer give as output a binary word formed by:

- timestamp, 64 bit unsigned integer

- baseline, 16 bit unsigned integer

- short integral, 16 bit unsigned integer

- long integral, 16 bit unsigned integer

- waveform, 16 unsigned integer for every sample

If we consider that at 20°C with a low threshold we can reach an event rate of 700Hz due to thermal noise. This rate is too high to be fully transcribed in the data storage. For this reason after the module that receives the data from the digitizer we put a module that analyses only the long integral(i.e. energy) and the PSD [1], and if these two value are lower respect a fixed threshold the event is discard. With this filter we can reduce the event rate from 700 Hz to 10 Hz. At this point we must to choose what we want to do with this data. With ABCD is possible to follow several approach, it is only necessary to create the appropriate module, that must be connected with the output filter.

The first approach is to save all the data in a binary raw file, called ADR [2]. This file contains the transcription of the entire data flow that come out from the digitizer or the filter, so it can be very heavy after a short time. This approach can be use when we need all the signal for the analysis or for debug the ABCD module, in fact after the data acquisition ADR file can be read by a simulator. The simulator substitutes the HV manager and acquisition server and generates simulated messages that fully reproduce the saved session [Fontana et al., 2018]. With this approach, if the events rate is of the order of 10Hz, we can acquire 1Gb data every day. Another way to analyse the data is to use the dedicated modules of ABCD, that allows to save only the main parameter of the single events that can be use for off-line particle discrimination, this is the approach use till now in the long data acquisition. In this case to have an idea, at 10Hz of events rate we acquire 1.5Gb of data for month.

For the determination of soil moisture content we are only interested in how many neutrons we detect in a fixed time interval. For this reason we can to create an ABCD module that receive the data from the digitizer, determine if the signal is a neutron or noise and after that save in a SQL file the neutron counts that we detected in a fixed time interval. With

---

[1]PSD:pulse shape discrimination, see section 3.6
[2]ADR: Abcd Data Raw

this approach, at 10Hz of events rate, we acquire 1Mb of data for month. So it's a very promising approach. In my thesis work I created the modules that can do on-line analysis. The description of that modules are shown below.

3.3.2   Module for online analysis

In the previous section we underlined the importance of creating few ABCD modules for on-line analysis in order to reduce the amount of data that must be stored and to have real-time data. The set of modules that are used in the online analysis are called "Finapp Analysis". We are interested in the determination of the neutron rate, muons rate and gain correction. The four modules created are:

- Pre-analysis

- Discrimination

- Gain correction

- Rate determination

In the figure 3.14 is shown the module for the analysis, their interconnections and the description of how they work.

Pre-analysis

This module read the data from the socket *tcp://127.0.0.1:16181*. From here it download the event timestamp and the relative waveform which is contained in a data array. At this point from the signal the module extract all the informations that are useful for particle identification. The parameters necessary for the analysis like the integration gate for the energy determination are not written in the main C program, but they are reported in a JSON[3] configuration file. This is extremely useful because if we want to change some parameters we must only change the configuration file and not the Pre-analysis code that are less user friendly. When the signal was processed the module create a JSON data packet that contain all the informations of the event and it send the informations to a PUB socket.

---

[3]JSON:JavaScript Object Notation is an open standard file format, and data interchange format, that uses human-readable text to store and transmit data objects consisting of attribute–value pairs and array data types (or any other serializable value).

Gain correction

The next step is to implement the online PMT gain correction both in the case of muons and neutrons. For do that is necessary to introduce a FIFO[4] memory that save the data for the gain correction.

In the case of neutrons, in section 4.2 we discuss that the final counts rate are temperature independent due to the V_{out} correction of the HV module, but in order to have a more general structure, we decide to introduce a gain correction also for neutrons. The average temperature are stored in a FIFO and after a fixed time interval this data are read by the average temperature module that send the output to gain correction module.

In the case of muons counts we have to proceed as describe in section 4.3.1. We have to determine the ^{40}K and muon peak position hourly in order to do a recalibration of the energy spectrum. For this reason we must save the event energy in a FIFO module and every ten minute we must send the event that are acquire in the last hour at the gain correction module in order to determine the K_{norm} and M_{norm} for the energy recalibration. For greater clarity we report in figure 3.14 the chart flow and the interconnection with that module with the other describe before.

Discrimination

This module receives the data packet from the module pre-analysis and the parameter that must be use for the gain correction by the dedicated module. With these data this module execute a particle identification, based on some parameter that are previously tested, the event can be identify like a neutron, gamma, muon or noise. When the particle is identify the counter is increment by one, at some point, that can be choose in order to be much lower in the time integration of rate module, the number saved in the counter is send to the dedicated socket and then the counter is reset and the cycle restart. For give an idea the message is published in the PUB socket every 3ms and the integration time can be of the order of 1 hour. As in the previous case the module need a JSON file configuration.

Rate determination

The rate determination module receives the counts from the previous module and integrate that count in a specific time interval that can be set when the module start to work. The integration time is not based on the digitizer timestamp but on the timestamp of the computer in which ABCD is installed. This is due to the fact that the timestamp of the digitizer can accumulate delay if it is used for long time (i.e. week or month). The rate

---

[4]FIFO (First In, First Out) in computing and in systems theory, is a method for organising the manipulation of a data structure where the oldest (first) entry, or 'head' of the queue, is processed first

informations are stored in a SQL file, in which are save the time and count for every particle type.
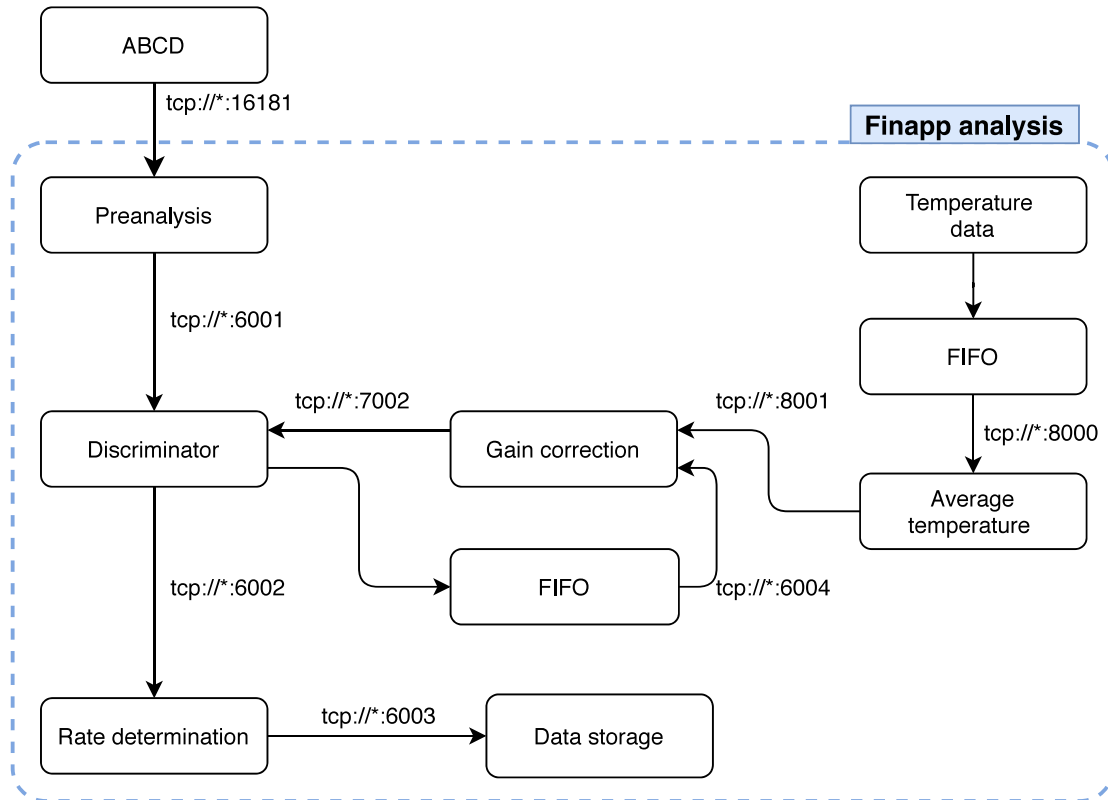
Figure 3.14: Structure and interconnection of the modules that are used for the online analysis with the gain correction module

3.4   Neutron discrimination

Before starting to analyse the data acquire in the field I developed a neutron discrimination algorithm. In fact as discuss before for the soil moisture estimation we use the neutron rate that are counted by the detector. Obviously the scintillator can interact not only with the neutrons, but also with gamma. Events acquired with the detector are composed by neutrons, gamma and noise due to thermal excitation of the PMT. For this reason it is important to develop several filters in order to be able to select only the neutron event. To create appropriate filters it is important to have some reference signals from neutrons. We acquire a data set with a neutrons source of ^{252}Cf a meter away from the detector. Moreover we add a lead shield to stop gamma ray and a polyethylene shield to thermalize fast neutrons generated by the neutron source. A second measurement was carried out without ^{252}Cf to have reference signal noise signals. In the first approach we analyse some

events that are present in the two data set. All the event can be divide in three different group:

- low energetic signal, generated by thermal excitation, that must be discarded because they are noise

- signals that have a very short tail, that can be associate to gamma ray

- signals with a very long tail, that can be associate to neutron interaction

In figure 3.15 are reported two different signals, one generated by gamma ray (3.15a) and the other by a neutron (3.15b).

(a) *Gamma signal*
**(b)** *Neutron signal*
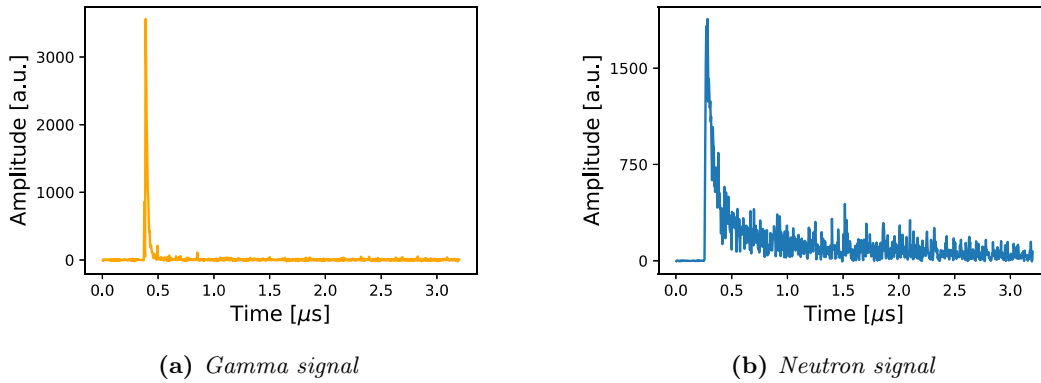
Figure 3.15: Example of different signal

As we expect the main difference is that the neutron signal have a very long tail respect to a gamma signal. In some case we notice that a neutron signal can be long enough to triggered another signal in the acquisition. The result is two consecutive events that are generated by the same neutron. An example are show in figure 3.16.
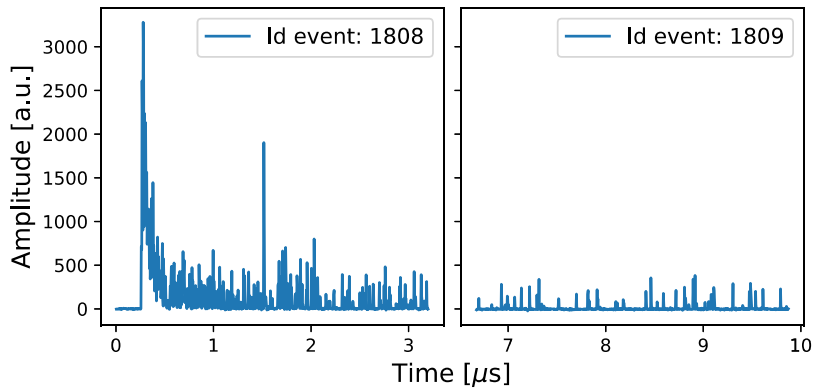
Figure 3.16: Example of a very long signal that for the data acquisition is recognized as two different events
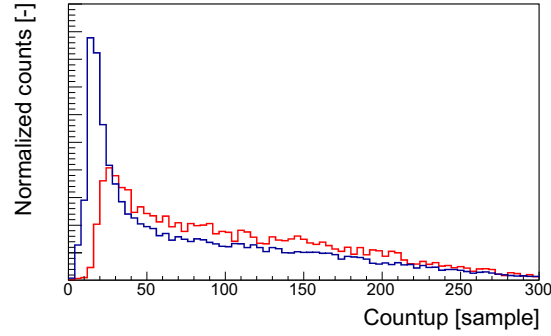
Figure 3.17: "Countup" distribution in two different data acquisition. The red histogram is an acquisition with ^{252}Cf. In blue without neutron source. The two histogram are normalized by the entries number.

For avoid that we put a limit of time difference of two consecutive events. We set that the time difference of two consecutive events can not be less that 10μs. In other word we put a limit of the data acquisition rate at 10kHz, that are several order of magnitude higher respect to the neutron rate that are the order of 10Hz.

3.5   Countup

In figure 3.15 we can notice that in the neutron signal after the first peak, the signal does not go to zero immediately. For this reason we introduce a parameter, called "countup" that represent the number of bin that are higher than a fixed threshold. We fix this threshold at the 50% of the hardware threshold, selected in the digitizer. In figure 3.17 we report the "countup" that we found in the two data acquisition. As we can see in the case of the acquisition with the ^{252}Cf source the events have an higher "countup" respect to the other acquisition. For this reason we can deduce that in average the neutron signal have at least a "countup" grater than 20.

3.6   Pulse shape discrimination

The pulse shape discrimination can be used for particle identification. This tecnicque is based on the time dependence of scintillation pulses when exited by radiation of different type. As it is show in figure 3.18 the scintillator alpha particle signal have a greater decay time respect to a gamma signal. This can be use for particle discrimination. The quantity that can be determine is called PSD, define in equation 3.4, where Q_{long} and Q_{short} are respectively the total and the partial integral. An example of these integration intervals are show in figure 3.18.
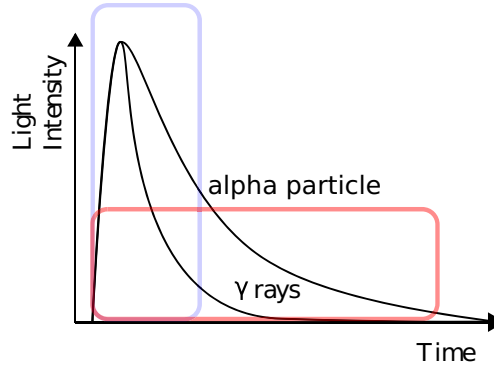
Figure 3.18: Time dependence of scintillator pulses when exited by radiation of different type. In blue is highlighted the short integration gate and in red the long integration gate.

$$PSD = \frac{Q_{long} - Q_{short}}{Q_{long}} \qquad (3.4)$$

In our case we choose to set the Q_{short} gate at 100 samples and the Q_{long} gate at 600 samples. These gates are optimized by the figure of merit (FoM). This is a quantity used to characterize the ability of the PSD parameter to discriminate alpha particle from gamma. As we ca see in figure 3.19 there is a well define division between the gamma and the neutrons. So we decide to identify as neutrons only the events that have a PSD greater than 0.4.
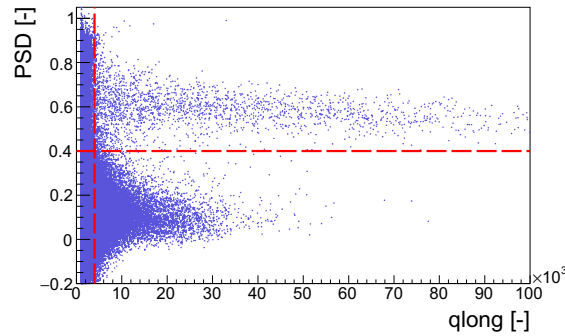
Figure 3.19: PSD versus qlong. The horizontal line indicate the separation between gamma signal and neurons signal. The red vertical line indicate the lower limit of qlong, under that limits is impossible to do a particle identification

Another important limits that we introduce, based on figure 3.19 is to delete all the event that have a qlong smaller than 4k, because we notice that these events are too small for applying any filter.

3.7   Integral rise time

Another parameter that we try to use is the integral raise time. In many cases the raise time of a signal or a integral curve is define as the time that it takes to pass from 10% to 90% of the maximum. In this case we define four different raise time integral that we call "cumul". The definition of the four cumuls are show in table 3.5.

Name	Limits
1	[0.05-0.50]
2	[0.50-0.95]
3	[0.05-0.70]
4	[0.30-0.95]

Table 3.5: Cumul definition. The limits indicate the lower and upper limits in percentage of the integral maximum.

After define these cumul we plot them, one in function of the other and we notice that in two particular cases the cumul of the events acquired with the ^{252}Cf create a regular pattern. As we can see in figure 3.20 neutron events are present in well define region, for this reason we have to find a method that is useful to select this area. The most reliable method is to find the center of the distribution and chose an optimal Mahalanobis distance, that are able to select properly this area.

(a) *Cumul 1 in function of cumul 4*   (b) *Cumul 2 in function of cumul 3*
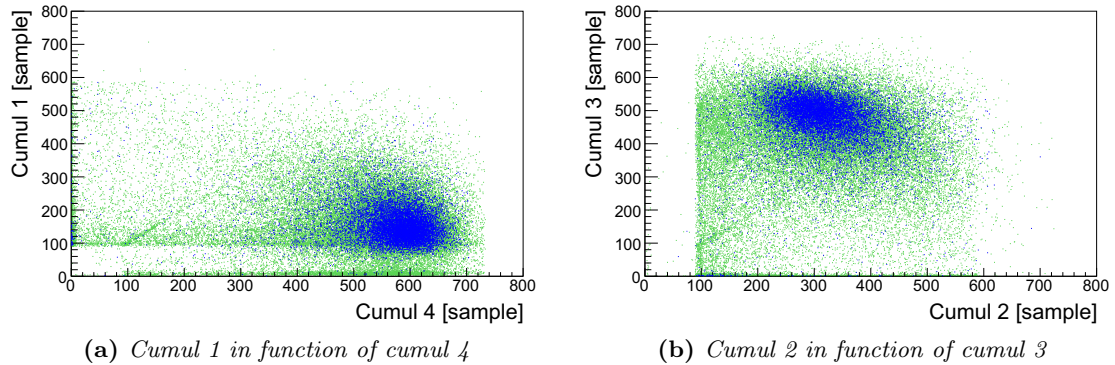
Figure 3.20: Distribution of different cumul of two different type of acquisition. The blue region are populated by event acquire with a ^{252}Cf source, while green region are a data acquisition without neutron source

Multivariate normal distribution   As we can see in this case we need a two dimensional distribution. So we decide to use the multivariate normal distribution that is a generalization of the one-dimensional normal distribution to higher dimensions [Wasserman, 2013]. In the specific 2-dim case the probability density function is the following:

$$f(x,y) = \frac{1}{2\pi\sigma_X\sigma_Y\sqrt{1-\rho^2}} \exp\left(\frac{-1}{2(1-\rho^2)}\left[\frac{(x-\mu_X)^2}{\sigma_X^2} + \frac{(y-\mu_Y)^2}{\sigma_Y^2} - \frac{2\rho(x-\mu_X)(y-\mu_Y)}{\sigma_X\sigma_Y}\right]\right)$$
(3.5)

Where μ_X and μ_y are the mean value of the variable X and Y, and ρ is the correlation. The Mahalanobis distance is a measure of the distance between a point P and a distribution D, introduced by f(x,y).It is a multi-dimensional generalization of the idea of measuring how many standard deviations away P is from the mean of D. The formal definition is:

$$D_M = \sqrt{(\mathbf{x}-\mu)^T\Sigma^{-1}(\mathbf{x}-\mu)}$$
(3.6)

where Σ is the covariance matrix. In our specific case we have

$$\mathbf{x} = \begin{pmatrix} x \\ y \end{pmatrix} \quad \mu = \begin{pmatrix} \mu_x \\ \mu_y \end{pmatrix} \quad \Sigma = \begin{pmatrix} \sigma_x^2 & \rho\sigma_x\sigma_y \\ \rho\sigma_x\sigma_y & \sigma_y^2 \end{pmatrix}$$
(3.7)

So at the and we obtain that the Mahalanobis distance in the 2-dim case is:

$$D_M = \sqrt{\frac{1}{1-\rho^2}\left[\frac{(x-\mu_x)^2}{\sigma_x^2} + \frac{(y-\mu_y)^2}{\sigma_y^2} - 2\rho\frac{(x-\mu_x)}{\sigma_x}\frac{(y-\mu_y)}{\sigma_y}\right]}$$
(3.8)

Going back to the cumul case, we fit the region of ^{252}Cf event, the blue zone in figure 3.20, with the function 3.5 and with the parameters that we obtain we check if the Mahalanobis distance from the center of the distribution is less than a fixed quantity, D_M. For example if we fix D_M=3 we obtain, all the events that have a D_M smaller than 3. The application of this cut is show in figure 3.21.

(a) *Cumul 1 in function of cumul 4*   **(b)** *Cumul 2 in function of cumul 3*
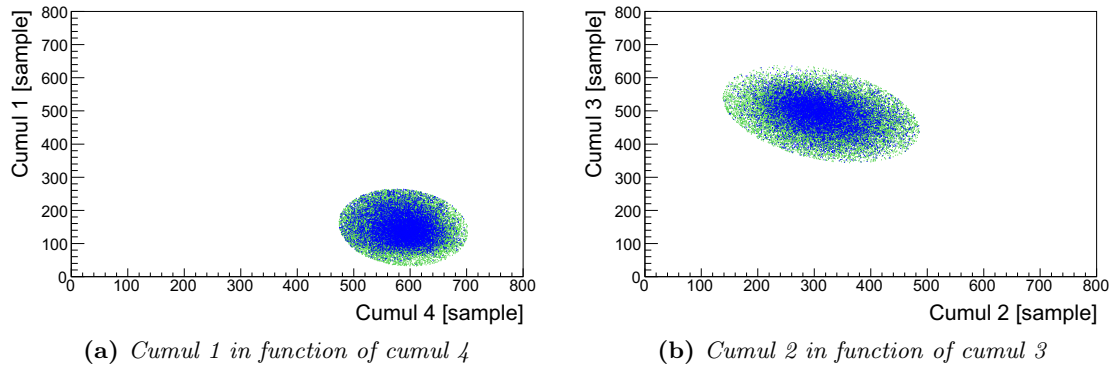
Figure 3.21: Example of cut with D_M=3

Chapter 4

Finapp measurement

In the previous section I described in detail the novel instrument that can be used to determine the soil content with the CRNS technique. In this chapter I will show the results from in the field applications.

4.1 Casalserugo data

From August 9th 2019 to December 4th 2019, the Finapp module was placed in Casalserugo (-PD-). In this data acquisition we didn't acquired the entire waveform but only the main parameters that we used in the offline analysis in order to do the neutron discrimination described before. We determine the hourly counts and we correct it with the average hourly pressure. For the correction we use the relation written in section 2.5 and a β=0.0076 as reported in [Stevanato et al., 2019]. After that we resample the counts, passing from hourly to daily counts in order to reduce the statistical fluctuation and to see if the fast neutrons counts are anti-correlated with the soil moisture. The main results are show in figure 4.1.

In figure 4.1 there are the normalized daily neutron rate without correction (blue line) and with pressure correction (orange line). The data interruptions in October is due to problem in the neutron detector. In the third panel is reported the pressure determine by the sensor placed near the detector. The rainfall data has been taken from the ARPAV [1] whether station placed in Legnaro, that are 6 Km far away from Casalserugo.

As we can see the pressure corrected neutron counts are correlated to the rainfall data. In particular we can notice that there are a little drop in counts in the first part of September and a greater one in November. There is not a counts variation in October 3rd, when 34 mm of rain fell. This can be due to the fact that the rainy event is localize in Legnaro and
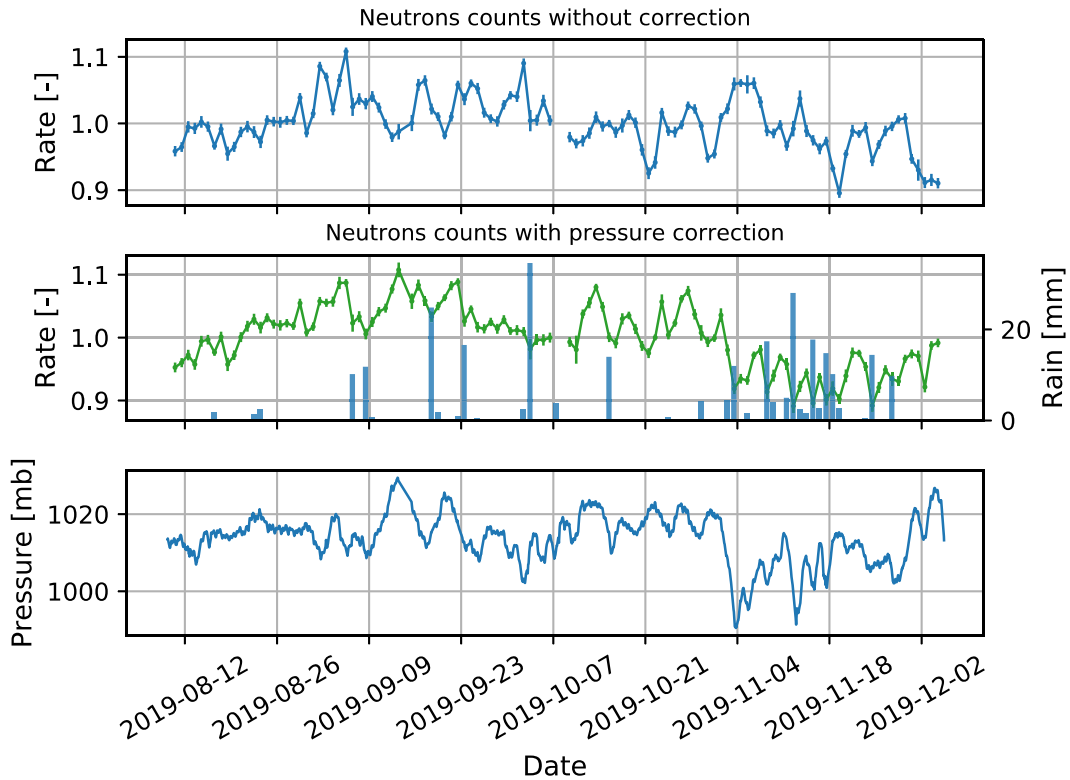

Figure 4.1: Normalized daily neutron counts detected in Casalserugo. In the first panel there are the counts without correction. In the second panel there are the counts with the pressure correction, in this panel are also reported the rainfall data. In the last panel there are the pressure data.

not in Casalserugo that is 6 Km far away. In conclusion we can say the CRNS can be used as a technique for measuring the soil moisture although with this apparatus a reduction in statistical fluctuations may help to better determine the soil moisture content. In the following section we try to study how the environmental temperature and variation in the incoming cosmic ray flux can affected the neutron counting and how to correct them.

4.2 Climate chamber

In this section we discuss how the temperature variation can affects the instrumental apparatus. For this reason we use a climate chamber. The climate chamber is located in "Polo didattico" of the physics department. The temperature can be set from -30°C to +70°C. In the first part of the study we put only the detector, the PMT and the temperature sensor in the climate chamber and we acquire data at: -10°C, -2°C, 5°C, 15°C, 23°C, 30°C and 37°C. The time acquisition can be change from 1 day, from several day, and it depends on the possibility of accessing the laboratory. From the data acquired

by the temperature sensor we can deduce that the time taken by the detector to reach the thermal balance is of the order of 3 hours after the temperature setting, for this reason in every data acquisition we discarded the first three hours of data. In order to compare the different acquisitions that have different durations we study the counts rate are expressed in counts/hours and we correct the counts with the pressure factor correction f_p (eq. 2.10) and β=0.0076.
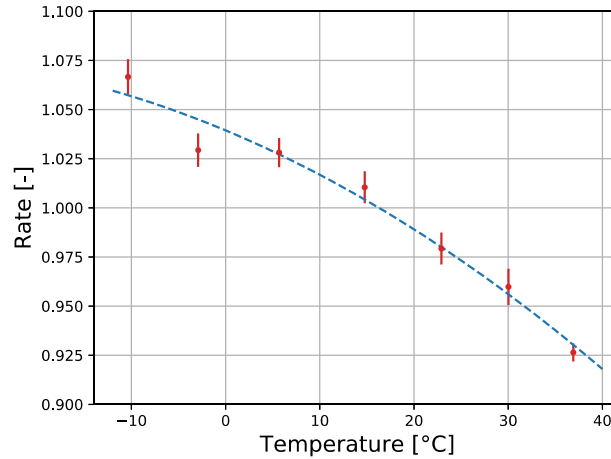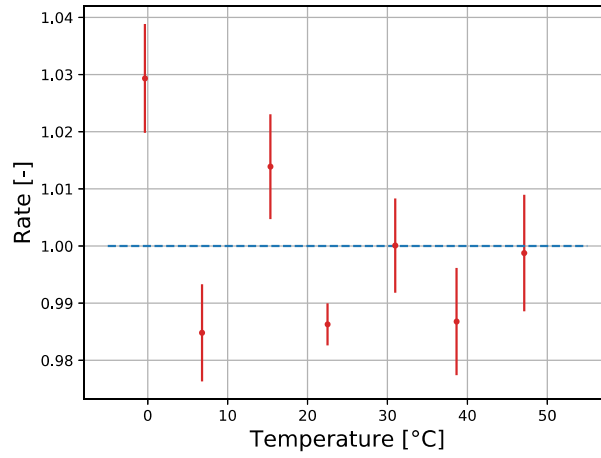

Figure 4.2: Normalized rate in function of climate chamber temperature. The data are fitted with a function $f(T) = a_0 + a_1 T + a_2 T^2$ with a_0 =1.04, a_1 = -1.99 $\cdot 10^{-3}$ and a_2=-2.59$\cdot 10^{-5}$

In figure 4.2 are show the main results. In the graph we can see that when the temperature increases the PMT gain decreases, consequently the number of neutrons that we found decrease. From -10°C to 37°C we notice a variation of the order of 14%. The data can be fitted by a second degree polynomial, and this parameter can be used in the future for a temperature correction.

Finished this part we decided to put all the apparatus (detector, HV module, digitizer and BeagleBone) in the climate chamber, in order to study if something change. In this configuration we record the V_{out} of the HV module in order to determine if the V_{out} is temperature dependent. In this configuration we acquire data at this different temperature:0°C, 7°C, 15°C, 22°C, 30°C, 37°C and 45°C. We try to acquire data at 55°C but it is impossible because we notice that when we exceed the temperature of 53°C the digitizer switches off due to thermal protection.

The main results of this second data acquisition are show in figure 4.3. As we can see the fluctuation respect to a reference value is less than 3% respect to 14% in the previous case. This is due to the fact that the HV module change the V_{out} as a function of the temperature as show in figure 4.4. This variation are useful for the PMT gain stabilization.

The additional fluctuation that we see in figure 4.3 can be associated to a correlation between the PMT gain and the discrimination algorithm, due to the fact that is difficult

Figure 4.3: Normalized rate in function of climate chamber temperature.
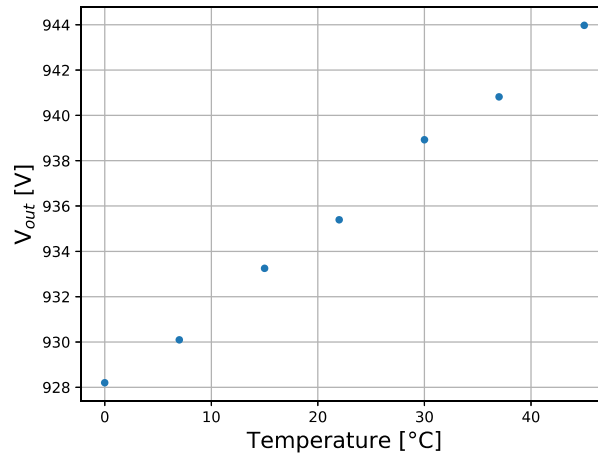
Figure 4.4: Temperature dependence of high voltage module V_{out}

to discriminate the signal that have low energy. With the increase of Ej-426 sheet we hope to disentangle this correlation.

4.3   Muon flux

In section 2.5 we reported that the neutron flux must be corrected due to the fluctuation of the incoming cosmic ray flux. For do that is possible to use the data of the nearest station of the Neutron Monitor Database (NMBD). In [Stevanato et al., 2019] is reported that this data can introduce errors in the determination of the incoming flux for several reason:

- the distance between the CNRS probe and NMDB stations may be of the order of several hundreds of km

- delays in collecting data from the NMDB can create problems for online monitoring

- dependence from an external source of information, the availability of NMDB data is at the discretion of the institution that maintains the station.

For this reason we put near the neutron detector a plastic scintillator to detect the muons (μ). Their flux at sea level depends on atmospheric conditions and incoming cosmic-ray fluctuations, in the same way as high-energy neutrons [Stevanato et al., 2019]. In order to be able to discriminate the muon contribution on the total amount of signal that are collect by the detector we must integrate the energy spectrum in the range of [2.7,10] MeV. The problem is that the experimental apparatus is sensible to thermal changes, in particular the PMT. In fact the PMT gain is temperature dependent and if we use a fixed energy gate for discrimination gamma from muon we can introduce error, for this reason the fist step is to develop an algorithm that stabilise the PMT gain.

4.3.1 Stabilisation of PMT gain

The PMT gain is temperature dependent, in particular the PMT gain and the temperature are anti correlated, in fact when the temperature increases the efficiency of the photo-cathode decreases. We developed a technique in order to stabilize the PMT gain. For do that we analyse a dataset acquire in 2018 in Germany as a reference.

In figure 4.5 we can see that the data acquire at 30° C are shifted in the more energetic region due to the fact the at low temperature the gain is bigger. For a quantitative analysis is important to found a structure that can be easy follow. The two structure that we choose is the ^{40}K Compton edge at 1200keV and the muon peak at 8 MeV.

In order to determine better the position of the Compton edge in the two cases we subtract the continuous part of the spectrum using asensitive non-linear iterative peak (SNIP) clipping algorithms to estimate background describe in [Morháč and Matoušek, 2008]. This algorithm is implemented in the ROOT function "ShowBackground". An example of application of this algorithm is show in figure 4.6. In the panel 4.6a we can see in blue the original data, in red the background determine by the function "ShowBackground". In the panel 4.6b we can we see the result data after background subtraction. We can notice that the peak position of ^{40}K gamma can be easily determine after the background subtraction. We do not use the ^{208}Pb peak in the future analysis due to low statistic.

The function "ShowBackground" have some parameters to be set in order to optimize the subtraction. After some evaluation we found that the optimal parameters to use are: number of iteration equal to 10 and "BackSmoothing" equal to 3. After the optimization of this procedure we started to study the change in position of the ^{40}k peak in function of
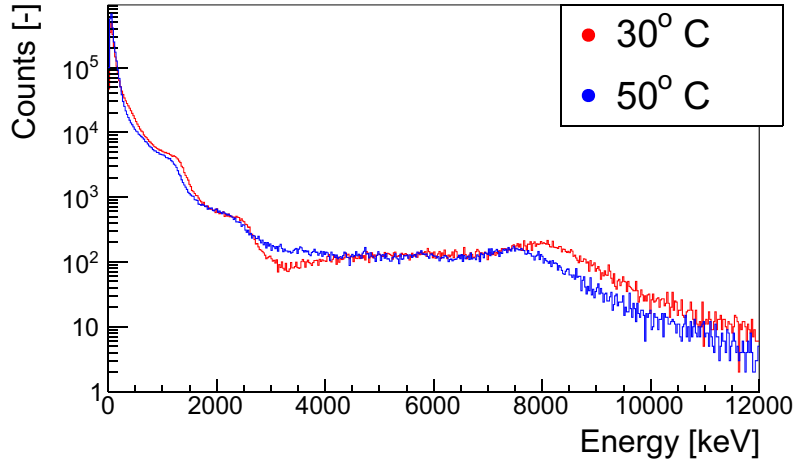
Figure 4.5: Superimposition of two data acquisition made at different environmental temperature in Germany.

**(a)** *Original spectrum signal*   **(b)** *Modify spectrum*
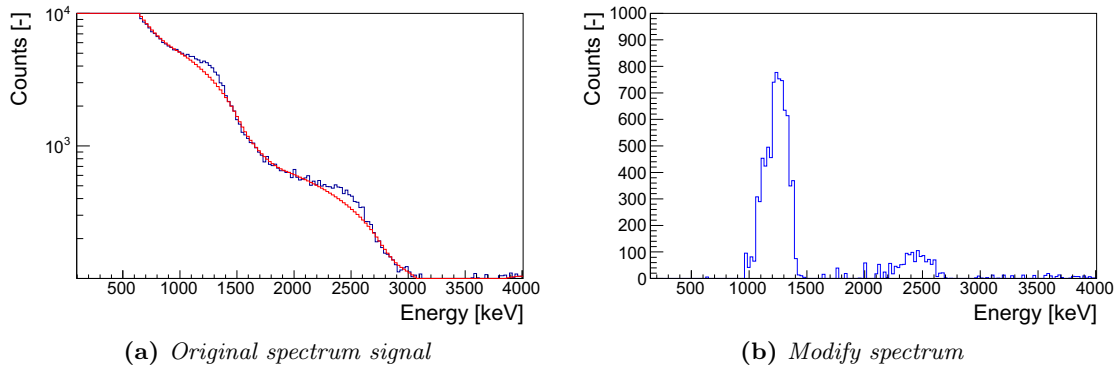
Figure 4.6: Example of background subtraction with the function "ShowBackground"

the temperature and we try to found an algorithm that can be useful for the stabilization of the peak. The tecnicque that we developed is based on moving average, in witch we use the peak position of the last hour in order to re-calibrate the ten minute that are after the hour. The parameters that we use for the calibration are called AVG_{norm}, that are the mean value of the K_{norm} and M_{norm}. This two parameters are the ratio of the theoretical ^{40}K and M_{norm} peak position determine by the Klein–Nishina formula and the position of the two peak in the selected hour. In figure 4.7, when we pass from the peak position without correction to the data with the correction we can notice that there is a reduction of temperature dependence of the peak position. With this algorithm we are able to obtain a better resolution of the ^{40}K position when the temperature change. In fact we can notice that the statistical fluctuation of the peak position can be reduce by a factor 1.6, like show in figure 4.8.

This stabilization of the peak position is really important if we want to determine an integral of the energy spectrum because we reduce the error that we make when we choose
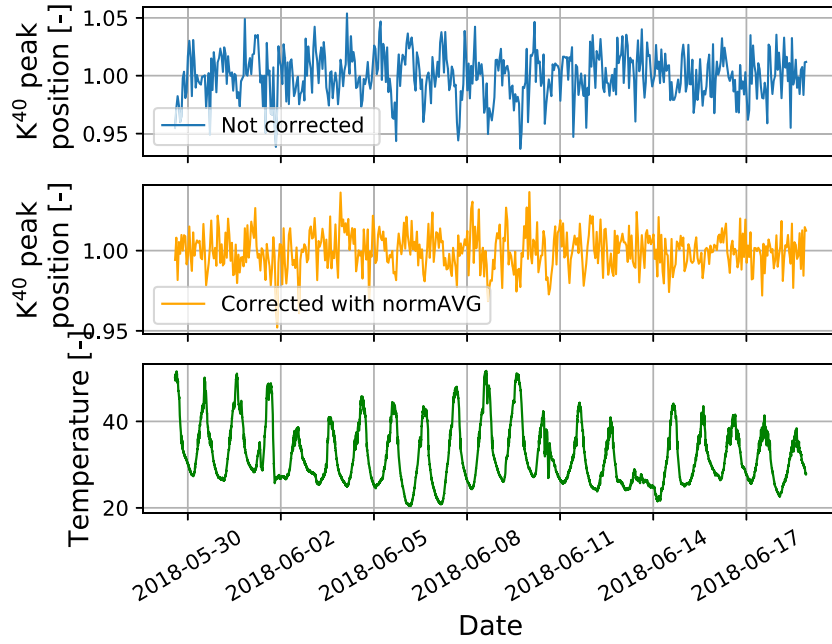
Figure 4.7: In the first panel we can see that the ^{40}K peak position is anti correlated with the temperature, that is reported in the third panel. In the middle panel is show the stabilization of the K^{40} by using the normAVG

(a) *Original K_{40} position signal*

(b) *Corrected K_{40} position*
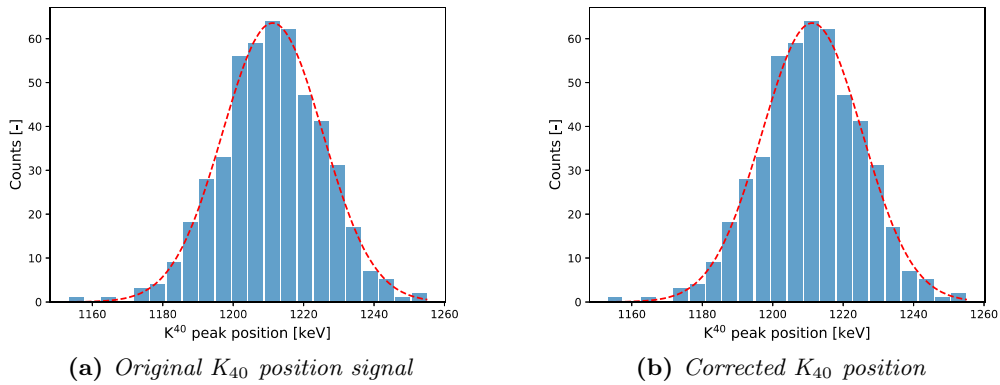
Figure 4.8: Comparison between the fluctuation of the ^{40}K peak position before the correction (FWHM= 55 keV) and after (FWHM= 33 keV)

the lower and upper limit of integration.

4.3.2 Cosmic muon rate

Before studying the historical series of muon flux we analyzed the energy spectrum of the acquire events, in order to set the optimal integration gate for the signal. In figure 4.9 is show an example the energy spectrum acquire by the plastic scintillator in May 2020. From this histogram we are able to determine the muon that hit the detector, in fact we can consider that all the events that have energy greater than 2.7 Mev are muons, for this reason we determine the integral from 2.7MeV to 10 MeV.
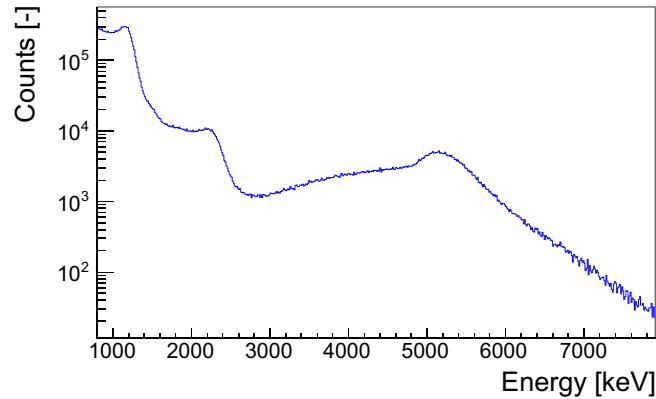
Figure 4.9: Energy spectrum of the plastic scintillator that we use for the muon detection.

We repeat this procedure for all the four different setup than we use, that are:

- From November 11th 2019 to December 4th 2019 we use a bigger plastic scintillator placed in Casalserugo (8m a.s.l), so the muon counts are higher respect the other case

- From November 14th 2019 to February 18th 2020 the data are acquired with a smaller detector that are placed in in Padova(12m a.s.l) in the last floor of Paolotti building

- From February 18th 2020 to March 2nd 2020 the smaller detector are moved in the climate chamber. It is located in the "Polo Didattico" situated in via Loredan on the ground floor.

- From March 9th 2020 to June 24th the detector is put back in Paolotti building.

The lack of data from March 3rd to March 8th is due to the fact that in this period it was impossible to reach the laboratory due to the regulations introduced to contain the pandemic of Covid-19.

In order to be able to compare the different setup we use corrective factor. In Casalserugo case it is a multiplicative factor due to the different detector size and the different elevation.

In case of the data acquire in the climate chamber the detector size are the same but we notice a a decrease in counts. The climate chamber is located in the "Polo Didattico"

situated in via Loredan on the ground floor.The cosmic muons must cross more concrete respect of Paolotti building. From some evaluation we can estimate that there are 60cm more concrete to cross in the climate chamber. In figure 4.10 we can deduce that with 60cm of concrete we have a reduction of 15% from the initial flux.
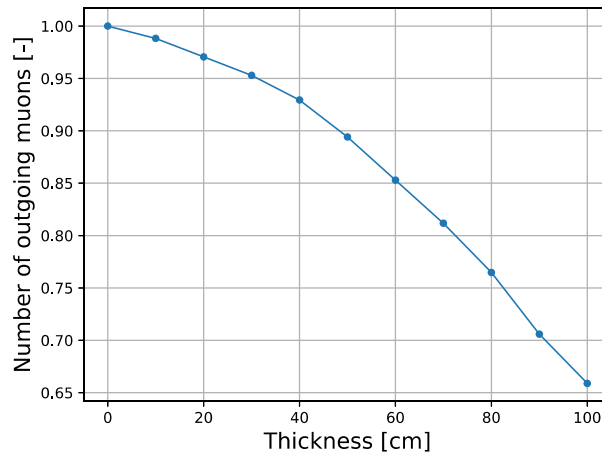

Figure 4.10: Normalize cosmic muon flux through concrete, from [Aguayo et al., 2011]

Another aspect that we notice in the muon flux in the climate chamber is that the muons peak is shift to le right, as show in figure 4.12. This phenomenon is a confirmation of the fact that the perpendicular flux of muon is shielded by the the concrete and we have more muons that arrive at the detector from other directions so they are able to release more energy in the scintillator. In fact as show in figure 4.11 the muons, that are not perpendicular to the detector, resale more energy in the scintillator due to the fact they cross more material.
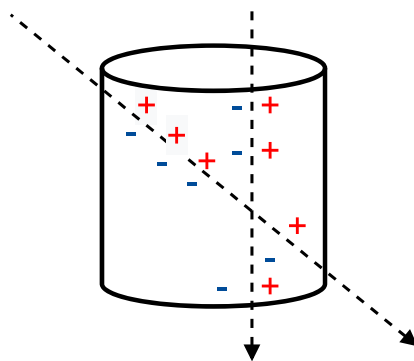
**Figure 4.11:** The muons that are not perpendicular cross more material respect to perpendicular ones, so their signal are more energetic.

After all this consideration we can conclude that also the muon rate of climate chamber must be corrected in order to be compatible with the other two data acquisition. For the correction of the incoming neutron flux we determine the rate of the cosmic muons every
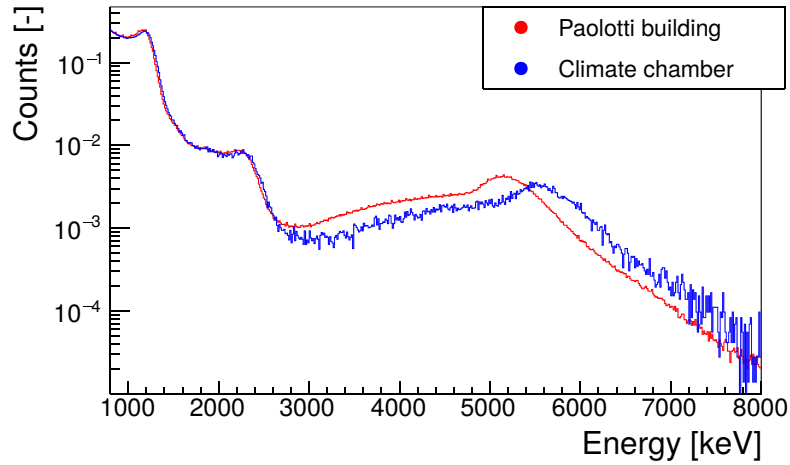
Figure 4.12: Comparison between the energy spectrum taken in "Paolotti building" and in the climate chamber. The spectrum is scaled by time acquisition.

hours and after that we determine the daily average muon rate, in figure 4.13 is normalize daily muon rate with and without pressure correction.
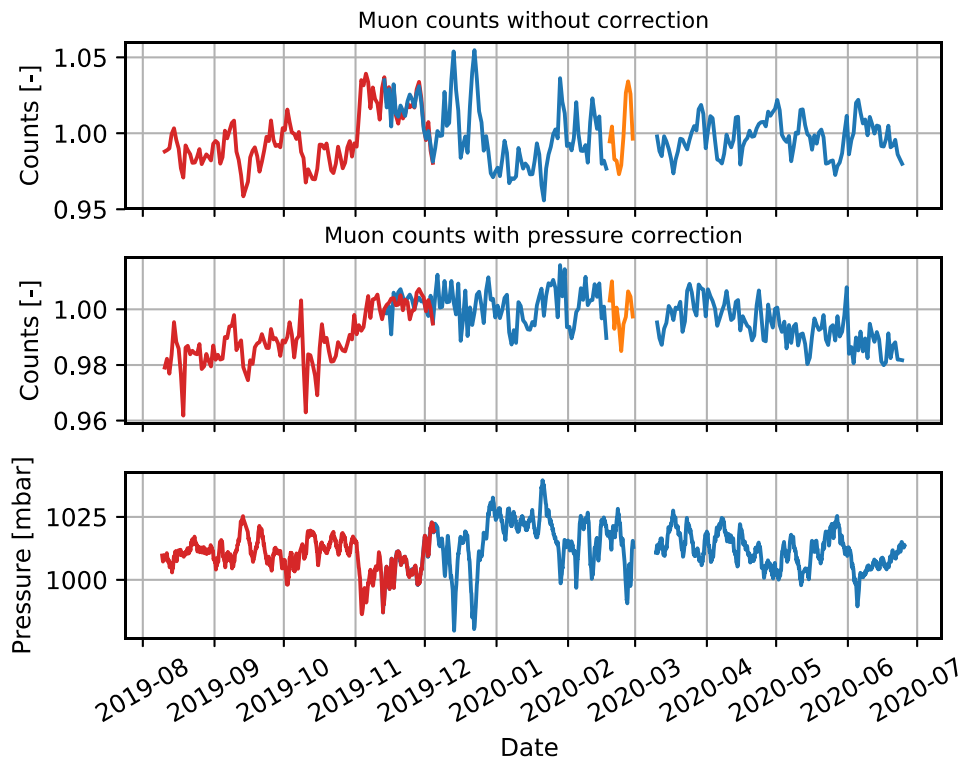

Figure 4.13: Muon rate acquire in Casalserugo (red line), Paolotti building in Padova (blue line) and "Polo Didattico" (orange line).

4.3.3 Attenuation coefficient for muons

Like for neutrons as discuss in section 2.5, also the muon flux is correlated with the atmospheric pressure:

$$f_P = exp(\beta(P - P_0)) \tag{4.1}$$

Where β is the barometric factor and P_0 is the reference pressure. As show in figure 4.14 the muon flux is higher respect to neutron flux and we can notice that the slope of the muon curve, in the region of 0 to 10 Km, is lower respect to neutron curve. For this reason we expect that the barometric factor for muons is lower respect to the neutron case.
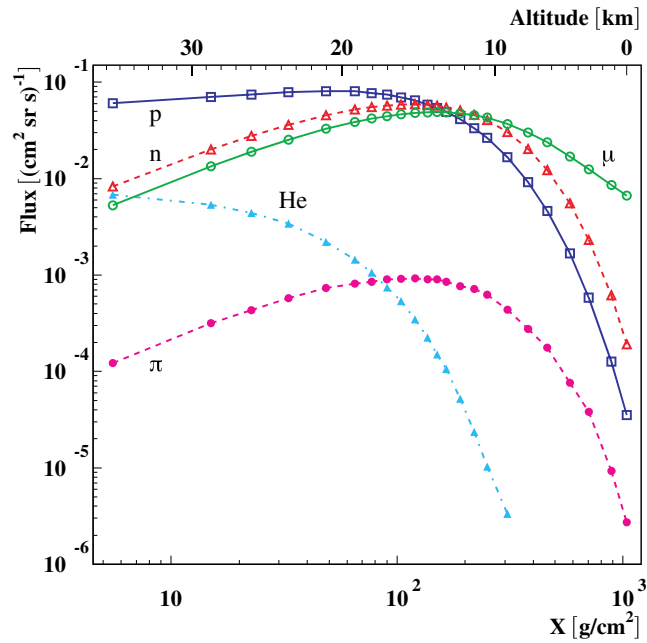

Figure 4.14: Total fluxes of muons, pions, protons, neutrons and helium nuclei as a function of atmospheric depth and altitude above sea level. The lines are drawn to guide the eye [Hansen et al., 2003].

With all the data collected in Casalserugo and Padova we are able to estimate the β value. We plot the daily muon counts in function of the average daily atmospheric pressure and we do a fit of the points with the equations 4.2.

$$log\left(\frac{M}{M_0}\right) = -\beta \cdot P + const \tag{4.2}$$

From the fit we obtain an attenuation factor $\beta = (183\pm6) \cdot 10^{-5}$. As expected the barometric factor in this case is lower respect the neutron case. The graphical results are show in figure 4.15.
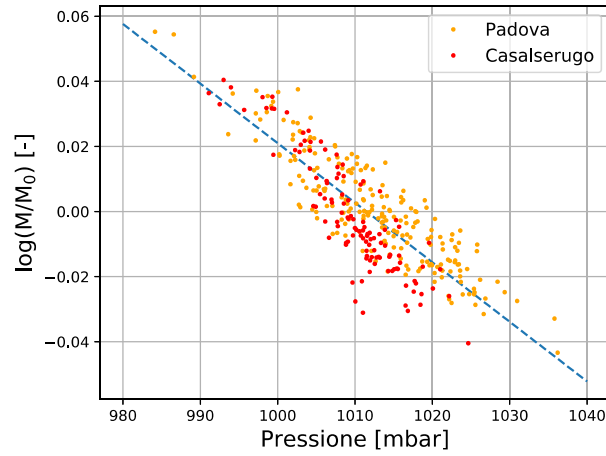
Figure 4.15: Normalized counts in function of the pressure. The data in orange are acquire in Padova, the other are collected in Casalserugo

In figure 4.14 we can also see that the slope of the muon flux change in function of the altitude. This can suggest that the β parameter is altitude dependent, this imply that when we want to correct the muon flux we must use the appropriate β. For this reason we do some data acquisition in different place that are more or less at the same latitude, in order to have the same magnetic rigidity. The place that we choose are reported in table 4.1. Moreover we report the position of the selected place in the map in figure 4.16.

Place	Start acquisition	End acquisition	Altitude a.s.l. [m]	P_{ref} [mbar]
Potsdam	March 2018	August 2018	40 m	1011
Pianaz	October 2019	November 2019	1296	859
Rifugio Città di Fiume	November 2019	December 2019	1918	802
Kaunertal	March 2019	August 2019	2626	755
Zugspite	December 2018	February 2019	2628	729

Table 4.1: Detail of the place in which we do the data acquisition

As we can see in the table altitude varies from 40m a.s.s to 2628m a.s.l. For every selected place we determine the P_{ref}, that is the average pressure that we determine during the data acquisition with the weather sensor.

In this acquisition we use a liquid scintillator, Ej-309, instead of plastic scintillator, consequently we changed the acquisition parameters in order to obtain compatible results. The other components remain the same, as in Padova case. The procedure to muon discrimination from gamma and stabilization of PMT gain due to temperature variation also remains unchanged.

As in the Padova case we report in a graph the daily muons counts in function of the
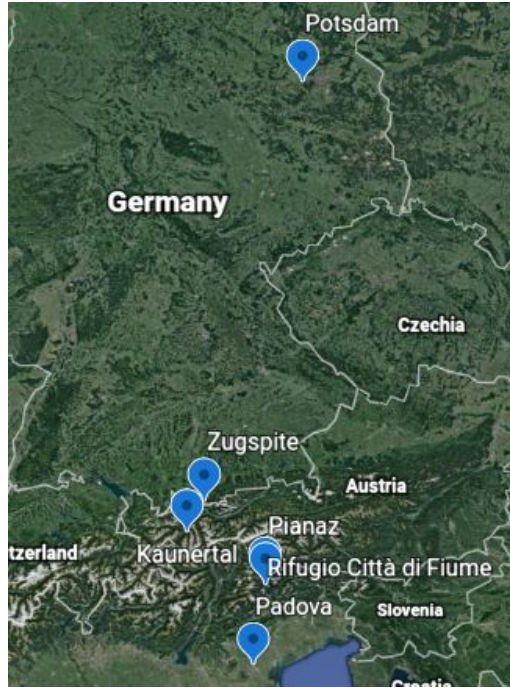
Figure 4.16: Maps of the place that we choose for the flux muon data acquisition at difference altitude

average daily pressure. After that we fit the data with the equation 4.2. The results are shown in figure 4.17. As expected we found that at low altitude there is a greater β.

At the end we put the barometric factor β as a function of the reference pressure that we found in the various acquisitions. The main result are show in table 4.2 and figure 4.18. We can notice that there is a strong correlation between the two quantity so we try to fit the data with a second degree polynomial. These data can be useful in the future to found an analytic relation that can be used to found the corresponding β of the place in which the CRNS probe will be placed, in order to correct the data for the incoming flux.

Place	Altitude a.s.l. [m]	P_{ref} [mbar]	β [10^{-5}mbar^{-1}]
Padova	12	1021	183±6
Potsdam	40	1011	209±8
Pianaz	1296	859	260±10
Rifugio Città di Fiume	1918	802	30±3
Kaunertal	2626	755	395±7
Zugspite	2628	729	430±10

Table 4.2: β value at different altitude
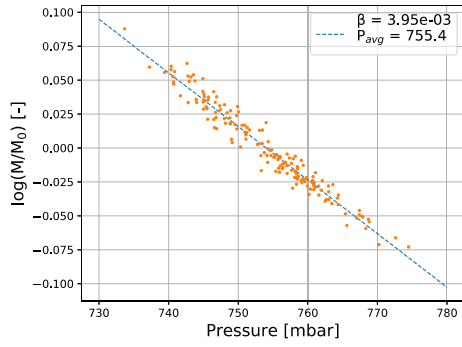
(a) *Kaunnertal*
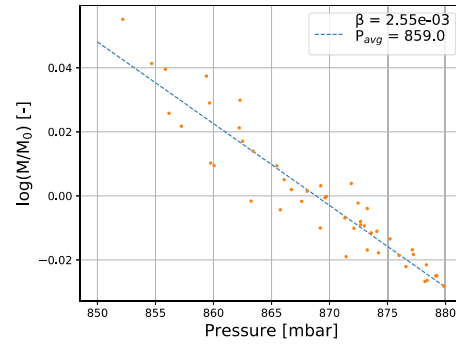
(b) *Pianaz*
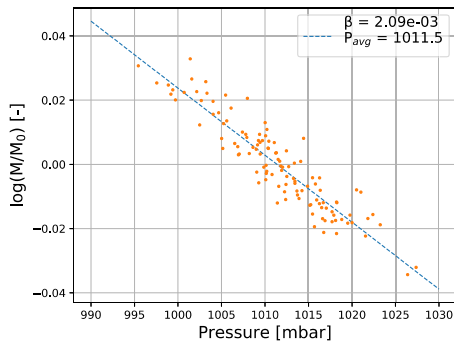
(c) *Potsdam*
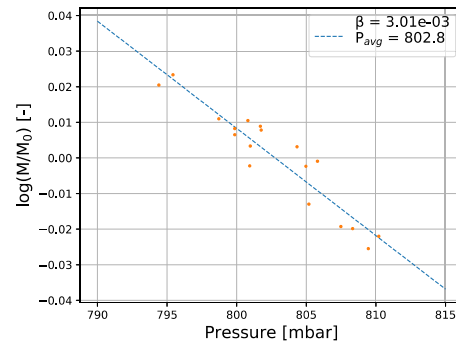
(d) *Rifugio Città di Fiume*
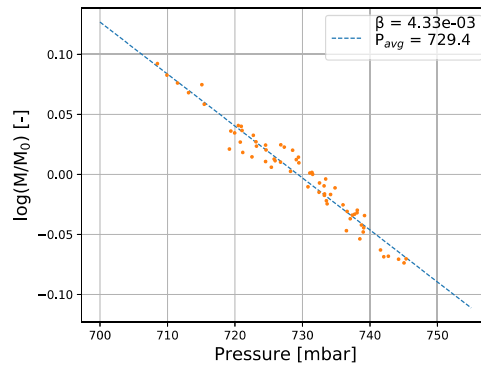
(e) *Mount Zugspite*

Figure 4.17: Normalize muon counts in log scale in function or the atmospheric pressure
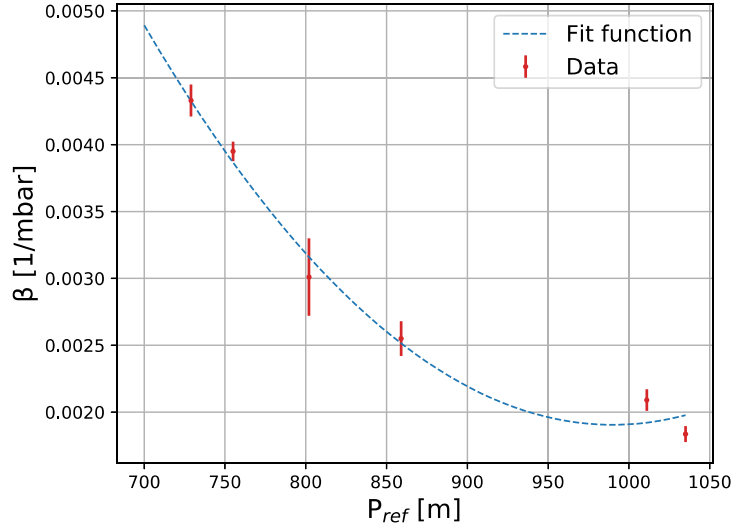
Figure 4.18: Correlation between β and P_{ref}. The fit function is a second degree polynomial $f(x) = a_2 \cdot x^2 + a_1 \cdot x + a_0$, with $a_2 = (3\pm1)\cdot10^{-8}$, $a_1 = (\text{-}7\pm2)\cdot10^{-8}$ and $(4\pm1)\cdot10^{-2}$

4.3.4 Temperature effect in cosmic muons flux

In addition to the pressure influence, atmospheric temperature changes produce significant intensity variations in muons flux. Temperature influences creation and disintegration processes of muons in the atmosphere. Generally, the temperature effect is described in two components:positive and negative. The positive effect is related to the temperature influence on pion decay, which is the major source of muons in the cosmic ray cascade process. The higher the temperature, the lower the atmospheric pion absorption, which implies a higher generation rate of muons [Duperieb, 1951]. In its turn, the negative effect is associated with changes of the muons average path along the atmosphere. It is expected that most muons are generated at higher altitude in summer due to the atmosphere expansion occurring during this period. Thus,they have a longer path to cross before reaching the ground,which allows more of them to decay, causing a decrease in their intensity at surface [Blackett, 1938].

Temperature variations also affect the cosmic ray intensity observed by the neutron monitors, but less significantly than in the case of muon detectors. The origin of this temperature effect is related to the fact that some of the neutrons generated in the cosmic ray shower are coming from pion/muon components.

In [De Mendonça et al., 2016] they analysed the temperature effect on the four ground muon detectors of the Global Muon Detector Network (GMDN). For the determination of the atmospheric temperature they used daily atmospheric temperature profiles obtained using data collected above each GMDN site by radio sondes onboard meteorological balloons and by the SABER (Sounding of the Atmosphere using Broadband Emission Ra-

diometry) instrument, which is on board the TIMED (Thermosphere, Ionosphere, Mesosphere Energetics and Dynamics) spacecraft.

As we can imagine the determination of the temperature with that instrument is complex, for this reason in this thesis work we try to found a correlation between the cosmic muon flux with the temperature acquire by ground temperature sensor. In in order to be sure that the change in cosmic muon flux is due only to atmospheric thermal expansion and not due to change in the incoming flux we decide to correct muon counts by the variation of incoming flux extracted from NMBD[2], that is temperature independent. From the database we choose some locations that have a magnetic rigidity greater than 4.4 GeV, like Padova. In particular we choose:

- Alma-Ata A (Kazakhstan): R_C=5.90 GeV, Altitude=897 m

- Athens (Greece): R_C=8.53 GeV, Altitude=260 m

- Baksan (Russia): R_C=5.70 GeV, Altitude=1700 m

- IGY Jungfraujoch (Switzerland): R_C=4.49 GeV, Altitude=3570 m

With the data that we found in the NMDB we do an daily average of the four selected stations and we correct the average daily muon counts using the equation 2.9, the results are shown in figure 4.19.

Obviously before do these corrections we do an hourly pressure correction, due to the fact that the pressure correction have the greater impact in the muons counts fluctuations.

In the figure 4.20 we report the weekly normalize muon counts acquire in Casalserugo (orange) and Padova (blue) in function of the average weekly temperature determine in the ARPAV weather station in Padova. As we can see there is a variation of muon counts from winter to summer by 2% and we can also see that the maximum of the counts is in correspondence of the temperature minimum as reported in [De Mendonça et al., 2016].

In order to better understand how much the two quantity are correlated, we choose another three ARPAV weather station and we found the correlation of the two quantities. One problem of Padova wheter station could be that the average temperature can be influenced by the urban environment. For this reason we choose these extra urban ARPAV stations:

- Legnaro (-PD-), altitude 7 m a.s.l, that station is located on the plain, but is less influenced by the urban environment

- Monte Grande (-PD-), altitude 465 a.s.l, situated in Colli Euganei

- Monte Cesen (-TV-), altitude 1552 m a.s.l, this station is in mountain so the temperature variations are similar to those found in high atmospheric conditions, and it is not affected by surrounding environment

---

[2]Neutron Monitor Database (NMDB) :`www.nmdb.eu/data`
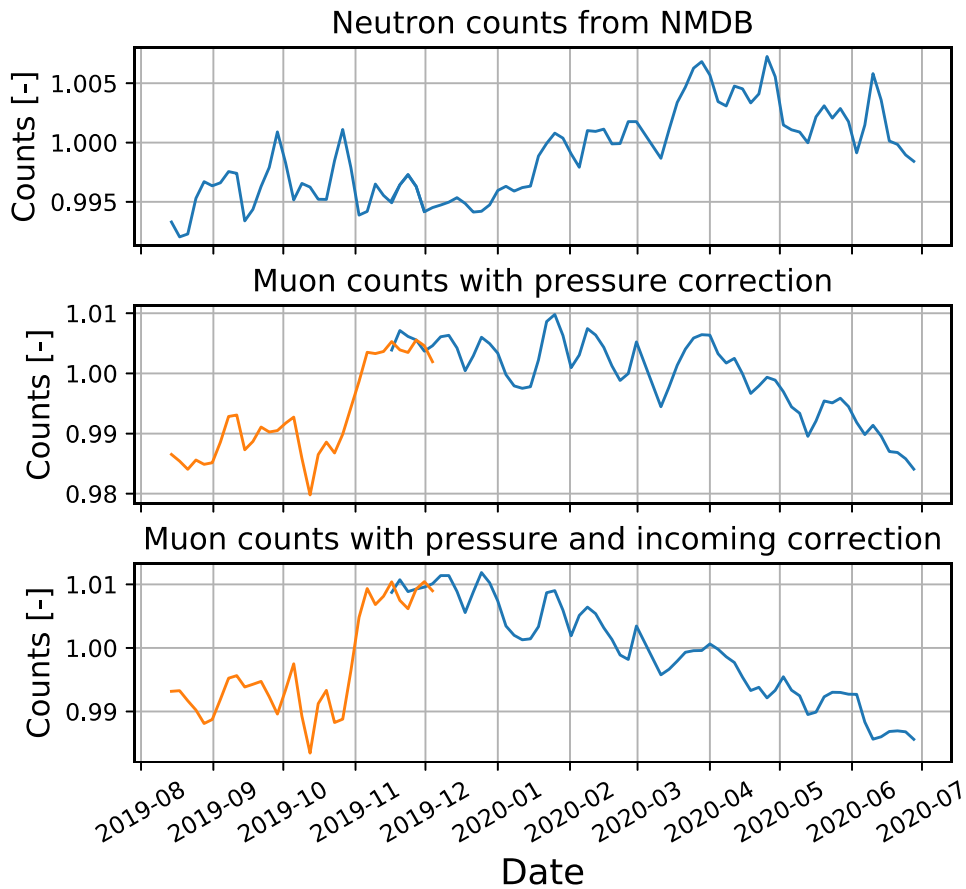
Figure 4.19: In panel one there are the weakly neutron counts from the NMDB.In the second panel there are the weakly muons counts determine in Casalserugo (orange) and Padova (blue) with the with Finapp apparatus. In the third panel there are the muon counts corrected with the incoming factor.

The main results are show in figure 4.21. As we can see the correlation between temperature and muon counts is good. It is not perfect due to statistical fluctuation. This result is very important because we are demonstrate that for study and quantify the temperature effects of the muons observed at the ground is not necessary to know the temperature at high atmosphere but the temperature from a weather station installed at ground. This result can be use for the correction of the muon counts in order to better determine the soil moisture content.
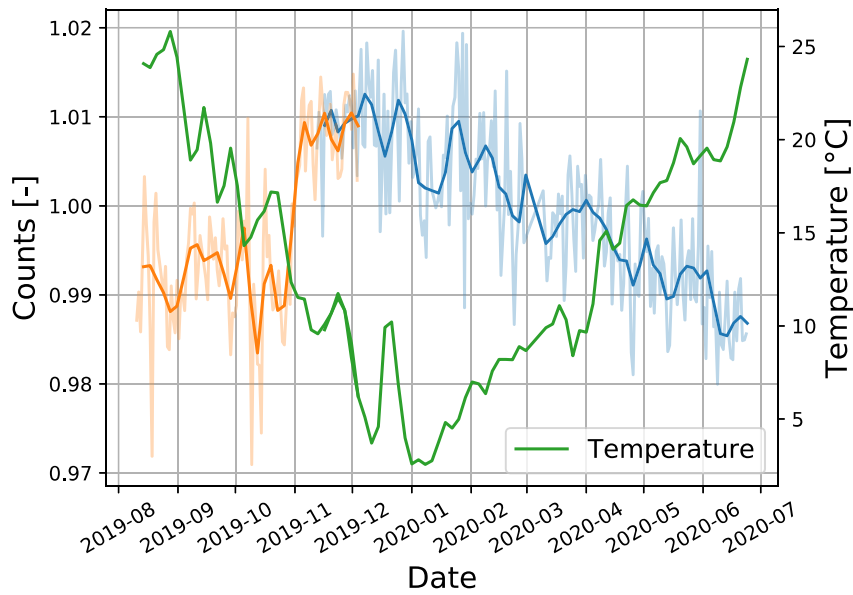
Figure 4.20: Weekly normalize muon counts acquire in Casalserugo (orange) and Padova (blue). In transparency are reported the average daily counts. The green line represent the weekly average temperature of Padova.
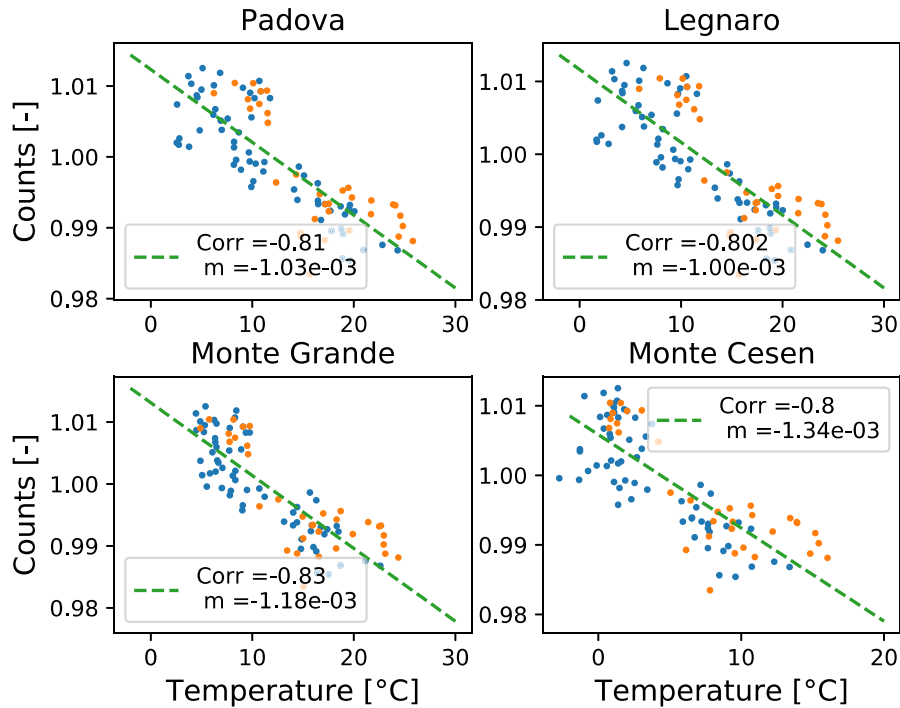
Figure 4.21: Correlation (Corr) between the muon counts and the temperature determined in different ARPAV weather stations. The data are fitted with a first degree polynomial, $Counts(T) = m \cdot T + cost$, (green dashed line).

4.4 Soil moisture estimation

In conclusion we try to determine the soil moisture from the neutron counts determine in Casalserugo. The counts have been corrected as described in 2.5, specifically we corrected the data with the barometric factor, the variations of the incoming flux and the temperature variations, using the result that we obtain in previous analysis. We pass from the neutron counts to the gravimetric soil moisture express in kg/kg using the following formula (see section 2.6 for more details):

$$\theta(N) = \frac{a_0}{\left(\frac{N}{N_0}\right) - a_1} - a_2 \tag{4.3}$$

With $a_0 = 0.0808$, $a_1 = 0.372$, $a_2 = 0.115$ and $N_0 = 1150$. The result are show in figure 4.22. We can notice that there is a correlation between the rainy event, which increase the soil moisture, with the estimation that we do with our instrumentation.
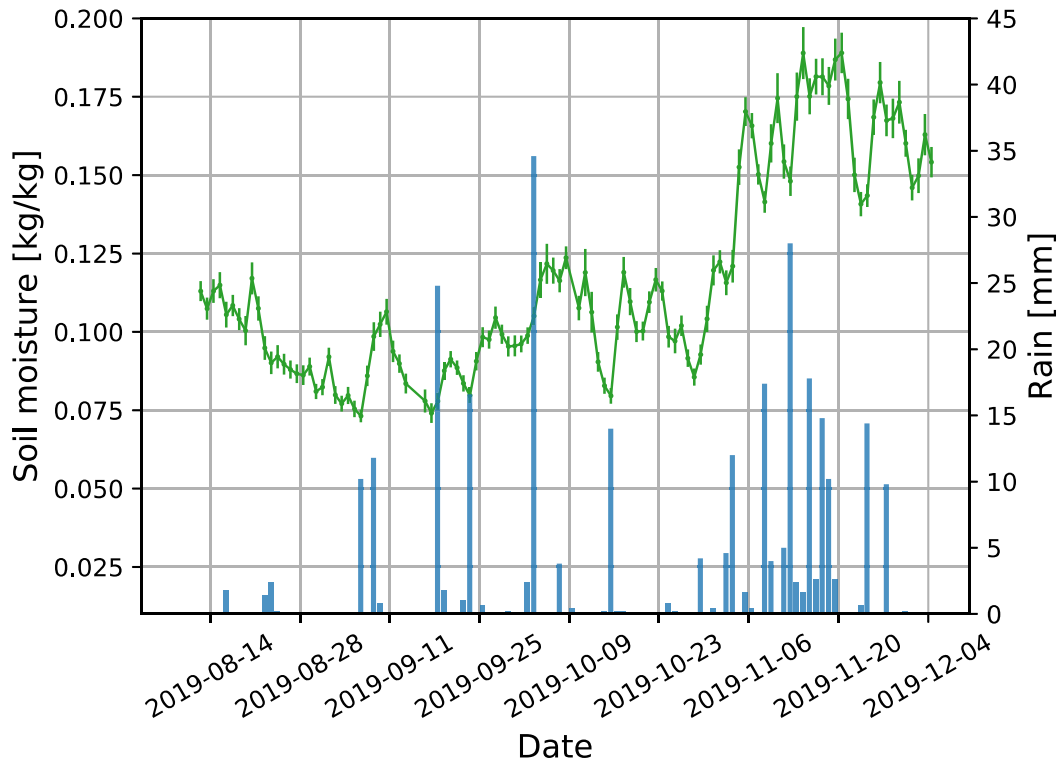
Figure 4.22: Soil moisture estimation determine with the CRNS tecnicque. The rainfall data are taken from the ARPAV weather station located in Legnaro.

4.5 Finapp 5

In conclusion of the thesis work we report some results of the new version of the neutron detector, called Finapp 5. As discuss before we must increase the efficiency of the neutron detector in order to reduce the statistical fluctuation in the counts. For do this we added two Ej-426 sheet in the detector and consequently we can use a bigger PMT. From calculation based on lithium content we expect an increasing of neutron counts by a factor 3.

(a) *Finapp 3*   (b) *Finapp 5*

Figure 4.23: Comparison between energy spectrum of two neutron detector configuration

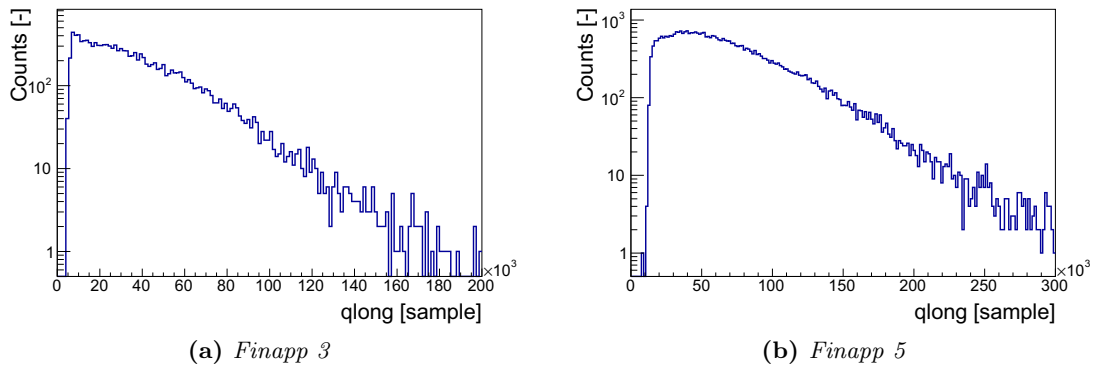In figure 4.23 we can see the comparison of two energy spectrum of neutrons acquire by the two different detector configuration. The acquisition was made at the same time in order to have the same environmental conditions. For the discrimination of neutrons in the Finapp 5 case we use the same parameter, describe in section 3.4, of the Finapp 3 configuration but with different threshold, due to the fact that we use a bigger PMT and there are more ^{6}Li. As expected the Finapp 5 have a neutron rate that are 3.16 greater that Finapp 3. In fact we obtain 2052 counts/hours in the first case and 649 count/hours in the second case. This is useful for statistical fluctuation reduction.

Another important aspect that we can see in figure 4.23 is that in the low energy region the two spectrum have a different shape. In the first case we can see that the neutrons have an exponential decay, in the second case there are a smooth structure. This is due to the fact that the discrimination algorithm work better in the Finapp 5 case at low energy. This is very important because we can disentangle the neutron counts from the low threshold choice and the temperature dependence of the neutron counts as discuss in 4.2.

Chapter 5

Conclusion

In my thesis work I try to study and develop a novel neutron detector for soil moisture estimation using the cosmic ray neutron sensing technique, which is based on ability to the hydrogen stored in water molecule to thermalize fast cosmic neutrons. I use an inorganic scintillator made of lithium-6-fluoride and zinc sulfide phosphor (ZnS:Ag), it is an efficient detector for thermal neutrons with low sensitivity to gamma radiation. This detector is proposed as an alternative to the current ^{3}He proportional counters used in this context, because the ^{3}He difficult to find and produce.

In the first part I developed filters that are able to discriminate the neutrons from other signals. These filters are based on signal analysis. I used these filters in a data acquisition made in Casalserugo (-PD-) from August 2019 to November 2019. The main results of this analysis is that the neutron counts are correlated with the soil moisture, as discuss in section 4.1. From that results we start to study how the temperature can affect the setup. For this reason we put the detector in a climate chamber. The main result is that the HV module are able to compensate the PMT gain change due to thermal effects. The residual fluctuation that we observe are mainly due to temperature dependence of the discrimination algorithm that can be analyzed in future studies.

In the second part I focus my attention on the fact that the neutron flux must be corrected by the incoming cosmic ray flux, as describe in section 2.5. For this reason I analysed several data acquisition made with a plastic scintillator that are able to detect muons. As in the neutron case the muon rate is temperature dependent, for this reason the first step is to remove this effect in the data, we developed a technique that is based on the tracking of the ^{40}K peak, for more detail see section 4.3.1. After I analysed the data acquire from August 2019 to July 2020. From this data I extrapolate the barometric factor for the muon flux correction. Afterwards I repeat this analysis for several data acquisition made at different altitude and I confirmed the altitude dependent of the β value, as reported in [Hansen et al., 2003]. Another important aspect that I notice in the muon flux is, as describe in [De Mendonça et al., 2016], the seasonal compression and expansion of the

atmosphere due to thermal variation. In [De Mendonça et al., 2016] is reported that for reveal this effects is necessary to use the temperature of high atmosphere. In my work I demonstrate that this effect is visible also if I use the temperature measured at ground.

In the third part I update the acquisition software. In particular I developed and test four ABCD modules, that are able to do an online data analysis, useful to determine in real-time the neutron and muon counts and consequently soil moisture estimation.

In the last part I acquire some new data with the new setup version, in which two additional Ej-426 sheet have been added, in order to increase the detector efficiency and consequently reduce the statistical fluctuation. As expected the new version have a neutron rate that are 3.16 greater that older one. Another important aspect that we notice is that in the new version we can disentangle the neutron counts from the low threshold choice and the temperature dependence of the neutron counts.

Appendix A

Energy calibration of the organic scintillator

In section 3.2.1 we reported that due to low Z of scintillators constituents. The interaction of photons with matter it takes place through Compton scattering. The expected distribution of the Compton events is described by the Klein–Nishina formula [Knoll, 2010]:

$$\frac{d\sigma}{dE} = \frac{\pi r_e^2}{m_e c^2 \alpha^2} \left(2 + \frac{s^2}{\alpha^2 \left(1 - s \right)^2} + \frac{s}{1 - s} \left(s - \frac{2}{\alpha} \right) \right) \tag{A.1}$$

where E is the kinetic energy of the scattered electron, r_e the classical electron radius, $\alpha = h\nu/m_c^2$, $s = T/h\nu$ and $h\nu$ is the initial photon energy. The electron energy distribution is show in figure A.1.
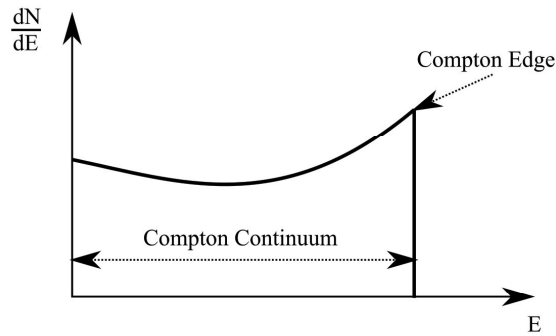
Figure A.1: Electron energy distribution

The main structure that we can found in the spectrum is the Compton Edge (EC). It position can easily found and it is describe by the following equation:

$$EC = 1 + \frac{h\nu}{1 + 2h\nu/m_o c^2} \tag{A.2}$$

Where $h\nu$ is the incoming photon energy. Due to the energy resolution of the organic scintillator we observe a Gaussian smearing of the predicted distribution [Stevanato et al., 2011] as show in figure .

Figure A.2: Computed distributions of Compton scattered events without (a) and with different Gaussian smearing corresponding to 5 (b), 10 (c), 15 (d) and 25 (e) keV pulse resolution.
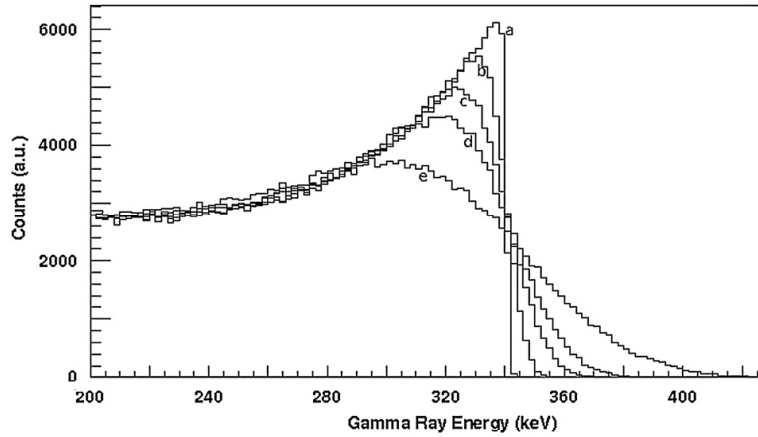
For this reason the procedure for a correct energy calibration of an organic scintillator is divided in the following steps:

1. measuring a high statistics pulse height distribution using a ^{22}Na gamma ray source, that emits two gamma ray at 511keV and 1274 keV [1].

2. producing a set of theoretical Compton distributions for the 511 and 1275 keV gamma rays with Gaussian smearing for different values of width

3. determining, by χ^2 analysis, the width that better reproduces the experimental distribution. The best-fit width value determines directly the energy shift of the nominal Compton Edge.

After finding the position of the two Compton edge we found a linear relation from the two EC and the data acquisition channel.

In conclusion every time that we change configuration we need a new calibration and we have to repeat the procedure describe above.

---

[1]Source:www.nndc.bnl.gov

Bibliography

[Aguayo et al., 2011] Aguayo, E., Kouzes, R. T., Ankney, A. S., Orrell, J. L., Berguson, T. J., Troy, M. D., et al. (2011). Cosmic ray interactions in shielding materials. *PNNL-20693, Pacific Northwest National Laboratory (July 2011)*.

[Aubert et al., 2003] Aubert, D., Loumagne, C., and Oudin, L. (2003). Sequential assimilation of soil moisture and streamflow data in a conceptual rainfall–runoff model. *Journal of Hydrology*, 280(1-4):145–161.

[Baroni et al., 2018] Baroni, G., Scheiffele, L., Schrön, M., Ingwersen, J., and Oswald, S. (2018). Uncertainty, sensitivity and improvements in soil moisture estimation with cosmic-ray neutron sensing. *Journal of Hydrology*, 564:873–887.

[Bettini, 2014] Bettini, A. (2014). *Introduction to elementary particle physics*. Cambridge University Press.

[Blackett, 1938] Blackett, P. M. (1938). On the instability of the barytron and the temperature effect of cosmic rays. *Physical Review*, 54(11):973.

[Brocca et al., 2017] Brocca, L., Ciabatta, L., Massari, C., Camici, S., and Tarpanelli, A. (2017). Soil moisture for hydrological applications: Open questions and new opportunities. *Water*, 9:140.

[Brocca et al., 2012] Brocca, L., Ponziani, F., Moramarco, T., Melone, F., Berni, N., and Wagner, W. (2012). Improving landslide forecasting using ascat-derived soil moisture data: A case study of the torgiovannetto landslide in central italy. *Remote sensing*, 4(5):1232–1244.

[Campos et al., 2018] Campos, I., González-Gómez, L., Villodre, J., González-Piqueras, J., Suyker, A. E., and Calera, A. (2018). Remote sensing-based crop biomass with water or light-driven crop growth models in wheat commercial fields. *Field Crops Research*, 216:175 – 188.

[De Mendonça et al., 2016] De Mendonça, R., Braga, C., Echer, E., Dal Lago, A., Munakata, K., Kuwabara, T., Kozai, M., Kato, C., Rockenbach, M., Schuch, N., et al. (2016). The temperature effect in secondary cosmic rays (muons) observed at the

ground: analysis of the global muon detector network data. *The Astrophysical Journal*, 830(2):88.

[Desilets and Zreda, 2003] Desilets, D. and Zreda, M. (2003). Spatial and temporal distribution of secondary cosmic-ray nucleon intensities and applications to in situ cosmogenic dating. *Earth and Planetary Science Letters*, 206(1-2):21–42.

[Desilets et al., 2010] Desilets, D., Zreda, M., and Ferré, T. P. (2010). Nature's neutron probe: Land surface hydrology at an elusive scale with cosmic rays. *Water Resources Research*, 46(11).

[Duldig, 2006] Duldig, M. (2006). Cosmic rays track the rotation of the milky way. *Science*, 314(5798):429–430.

[Duperieb, 1951] Duperieb, A. (1951). On the positive temperature effect of the upper atmosphere and the process of meson production. *Journal of Atmospheric and Terrestrial Physics*, 1(5-6):296–310.

[Ehlert et al., 2008] Ehlert, D., Horn, H.-J., and Adamek, R. (2008). Measuring crop biomass density by laser triangulation. *Computers and electronics in agriculture*, 61(2):117–125.

[Entekhabi et al., 2014] Entekhabi, D., Yueh, S., O'Neill, P., Kellogg, K., Allen, A., Bindlish, R., Brown, M., Chan, S., Colliander, A., Crow, W., et al. (2014). Smap handbook soil moisture active passive. *Mapping Soil Moisture Freeze/Thaw from Space, Pasadena, CA*.

[Fontana et al., 2018] Fontana, C., Carnera, A., Lunardon, M., Pino, F., Sada, C., Soramel, F., Stevanato, L., and Moretto, S. (2018). A distributed data acquisition system for nuclear detectors. *International Journal of Modern Physics: Conference Series*, 48:1860118.

[Hansen et al., 2003] Hansen, P., Carlson, P., Mocchiutti, E., Sciutto, S., and Boezio, M. (2003). Flux of atmospheric muons: Comparison between aires simulations and caprice98 data. *Physical Review D*, 68(10):103001.

[Heimovaara, 1994] Heimovaara, T. (1994). Frequency domain analysis of time domain reflectometry waveforms: 1. measurement of the complex dielectric permittivity of soils. *Water Resources Research*, 30(2):189–199.

[Hess, 1912] Hess, V. F. (1912). Über beobachtungen der durchdringenden strahlung bei sieben freiballonfahrten. *Phys. Z.*, 13:1084–1091.

[Hess et al., 1959] Hess, W. N., Patterson, H. W., Wallace, R., and Chupp, E. L. (1959). Cosmic-ray neutron energy spectrum. *Phys. Rev.*, 116:445–457.

[Hillel, 1998] Hillel, D. (1998). *Environmental soil physics: Fundamentals, applications, and environmental considerations.* Elsevier.

[Jakobi et al., 2018] Jakobi, J., Huisman, J., Vereecken, H., Diekkrüger, B., and Bogena, H. (2018). Cosmic ray neutron sensing for simultaneous soil water content and biomass quantification in drought conditions. *Water Resources Research*, 54(10):7383–7402.

[Knoll, 2010] Knoll, G. F. (2010). *Radiation detection and measurement.* John Wiley & Sons.

[Köhli et al., 2015] Köhli, M., Schrön, M., Zreda, M., Schmidt, U., Dietrich, P., and Zacharias, S. (2015). Footprint characteristics revised for field-scale soil moisture monitoring with cosmic-ray neutrons. *Water Resources Research*, 51(7):5772–5790.

[Kouzes, 2009] Kouzes, R. T. (2009). The 3he supply problem. Technical report, Pacific Northwest National Lab.(PNNL), Richland, WA (United States).

[Krane et al., 1987] Krane, K. S., Halliday, D., et al. (1987). *Introductory nuclear physics.*

[Mahmood et al., 2013] Mahmood, H. S., Hoogmoed, W. B., and Van Henten, E. J. (2013). Proximal gamma-ray spectroscopy to predict soil properties using windows and full-spectrum analysis methods. *Sensors*, 13(12):16263–16280.

[Massari et al., 2014] Massari, C., Brocca, L., Moramarco, T., Tramblay, Y., and Lescot, J.-F. D. (2014). Potential of soil moisture observations in flood modelling: Estimating initial conditions and correcting rainfall. *Advances in Water Resources*, 74:44–53.

[Morháč and Matoušek, 2008] Morháč, M. and Matoušek, V. (2008). Peak clipping algorithms for background estimation in spectroscopic data. *Applied spectroscopy*, 62(1):91–106.

[Nations, 2018] Nations, F. (2018). *Water for sustainable food and agriculture: A report produced for the G20 Presidency of Germany.* Food & Agriculture Org.

[Porporato et al., 2002] Porporato, A., D'odorico, P., Laio, F., Ridolfi, L., and Rodriguez-Iturbe, I. (2002). Ecohydrology of water-controlled ecosystems. *Advances in Water Resources*, 25(8-12):1335–1348.

[Robinson et al., 2003] Robinson, D., Jones, S., Wraith, J., Or, D., and Friedman, S. (2003). A review of advances in dielectric and electrical conductivity measurement in soils using time domain reflectometry. *Vadose Zone J.*, 2.

[Robock, 2015] Robock, A. (2015). Hydrology, floods and droughts — soil moisture. In North, G. R., Pyle, J., and Zhang, F., editors, *Encyclopedia of Atmospheric Sciences (Second Edition)*, pages 232 – 239. Academic Press, Oxford, second edition edition.

[Rosolem et al., 2013] Rosolem, R., Shuttleworth, W. J., Zreda, M., Franz, T., Zeng, X., and Kurc, S. (2013). The effect of atmospheric water vapor on neutron count in the cosmic-ray soil moisture observing system. *Journal of Hydrometeorology*, 14(5):1659–1671.

[Schmugge et al., 2002] Schmugge, T. J., Kustas, W. P., Ritchie, J. C., Jackson, T. J., and Rango, A. (2002). Remote sensing in hydrology. *Advances in water resources*, 25(8-12):1367–1385.

[Seneviratne et al., 2010a] Seneviratne, S., Corti, T., Davin, E., Hirschi, M., Jaeger, E., Lehner, I., Orlowsky, B., and Teuling, A. (2010a). Investigating soil moisture-climate interactions in a changing climate: A review. *Earth-Science Reviews*, 99:125–161.

[Seneviratne et al., 2010b] Seneviratne, S. I., Corti, T., Davin, E. L., Hirschi, M., Jaeger, E. B., Lehner, I., Orlowsky, B., and Teuling, A. J. (2010b). Investigating soil moisture–climate interactions in a changing climate: A review. *Earth-Science Reviews*, 99(3):125 – 161.

[Shiklomanov, 1998] Shiklomanov, I. A. (1998). *World water resources: a new appraisal and assessment for the 21st century: a summary of the monograph World water resources*. Unesco.

[Stevanato et al., 2019] Stevanato, L., Baroni, G., Cohen, Y., Cristiano Lino, F., Gatto, S., Lunardon, M., Marinello, F., Moretto, S., and Morselli, L. (2019). A novel cosmic-ray neutron sensor for soil moisture estimation over large areas. *Agriculture*, 9(9):202.

[Stevanato et al., 2011] Stevanato, L., Fabris, D., Hao, X., Lunardon, M., Moretto, S., Nebbia, G., Pesente, S., Sajo-Bohus, L., and Viesti, G. (2011). Light output of ej228 scintillation neutron detectors. *Applied Radiation and Isotopes*, 69(2):369 – 372.

[Störmer, 1955] Störmer, C. (1955). *The polar aurora*. Clarendon Press.

[Strati et al., 2018] Strati, V., Albéri, M., Anconelli, S., Baldoncini, M., Bittelli, M., Bottardi, C., Chiarelli, E., Fabbri, B., Guidi, V., Raptis, K. G. C., et al. (2018). Modelling soil water content in a tomato field: proximal gamma ray spectroscopy and soil–crop system models. *Agriculture*, 8(4):60.

[Tapley et al., 2004] Tapley, B., Bettadpur, S., Ries, J., Thompson, P., and Watkins, M. (2004). Grace measurements of mass variability in the earth system. *Science (New York, N.Y.)*, 305:503–5.

[Tian et al., 2016a] Tian, Z., Li, Z., Liu, G., Li, B., and Ren, T. (2016a). Soil water content determination with cosmic-ray neutron sensor: Correcting aboveground hydrogen effects with thermal/fast neutron ratio. *Journal of Hydrology*, 540:923–933.

[Tian et al., 2016b] Tian, Z., Li, Z., Liu, G., Li, B., and Ren, T. (2016b). Soil water content determination with cosmic-ray neutron sensor: Correcting aboveground hydrogen effects with thermal/fast neutron ratio. *Journal of Hydrology*, 540:923 – 933.

[Tramblay et al., 2010] Tramblay, Y., Bouvier, C., Martin, C., Didon-Lescot, J.-F., Todorovik, D., and Domergue, J.-M. (2010). Assessment of initial soil moisture conditions for event-based rainfall–runoff modelling. *Journal of Hydrology*, 387(3-4):176–187.

[Ütikofer et al., 2007] Ütikofer, R. B., Eo, F., and LÜCKIGER (2007). 30th international cosmic ray conference characteristics of near real-time cutoff calculations on a local and global scale.

[Wasserman, 2013] Wasserman, L. (2013). *All of statistics: a concise course in statistical inference.* Springer Science & Business Media.

[Wooldridge et al., 2003] Wooldridge, S., Kalma, J. D., and Walker, J. P. (2003). Importance of soil moisture measurements for inferring parameters in hydrologic models of low-yielding ephemeral catchments. *Environmental Modelling & Software*, 18(1):35–48.

[Zarco-Tejada et al., 2014] Zarco-Tejada, P. J., Hubbard, N., and Loudjani, P. (2014). Precision agriculture: an opportunity for eu farmers—potential support with the cap 2014–2020. *Joint Research Centre (JRC) of the European Commission.*

[Ziegler, 1996] Ziegler, J. F. (1996). Terrestrial cosmic rays. *IBM journal of research and development*, 40(1):19–39.

[Zreda et al., 2008] Zreda, M., Desilets, D., Ferré, T., and Scott, R. L. (2008). Measuring soil moisture content non-invasively at intermediate spatial scale using cosmic-ray neutrons. *Geophysical research letters*, 35(21).

[Zreda et al., 2012] Zreda, M., Shuttleworth, W., Zeng, X., Zweck, C., Desilets, D., Franz, T., and Rosolem, R. (2012). Cosmos: the cosmic-ray soil moisture observing system. *Hydrology and Earth System Sciences*, 16:4079–4099.